



Klein tunneling on Bour surfaces with N topological defects

V́ctor A. Gonźlez-Doḿnguez and Juan A. Reyes-Nava

*Instituto de Investigaci3n e Innovaci3n en Energías Renovables, Universidad de Ciencias y Artes de Chiapas, Libramiento Norte Poniente No. 1150, C.P. 29039, Tuxtla Guti3rrez, Chiapas, M3xico*Pavel Castro-Villarreal ^{*}*Facultad de Ciencias en F́sica y Matemáticas, Universidad Aut3noma de Chiapas, Carretera Emiliano Zapata, Km. 8, Rancho San Francisco, 29050 Tuxtla Guti3rrez, Chiapas, M3xico* (Received 12 July 2022; revised 10 March 2023; accepted 18 October 2023; published 14 November 2023)

The existence of a curved graphene sheet with the geometry of a Bour surface B_n is supposed, such as the catenoid (or helicoid), B_0 , and the classical Enneper surface, B_2 , among others. In particular, in this paper, the propagation of the electronic degrees of freedom on these surfaces is studied based on the Dirac model coupled to a non-Abelian gauge field that captures topological defects present on each of the surfaces. As a consequence of the polar geometry of B_n , it is found that the geometry of the surface causes the Dirac fermions to move as if they would be subjected to an external potential coupled to a spin-orbit term. The geometry-induced potential is interpreted as a barrier potential, which is asymptotically zero. Furthermore, the behavior of asymptotic Dirac states and scattering states are studied through the Lippmann-Schwinger formalism. It is found that for surfaces B_0 and B_1 , the total transmission phenomenon is found for sufficiently large values of energy, while for surfaces B_n , with $n \geq 2$, it is shown that there is an energy point E_K where Klein's tunneling is realized, while for energy values $E \gg E_K$ it is found that the conductance of the hypothetical material is completely suppressed. In addition, for a large number, N , of topological defects the transmission decays as N^{-2} as far as energy values are different than E_K .

DOI: [10.1103/PhysRevB.108.195421](https://doi.org/10.1103/PhysRevB.108.195421)**I. INTRODUCTION**

One of the intriguing properties of graphene, among many others [1,2], is that the charge carriers can be described by quasiparticles with the same behavior as relativistic Dirac fermions at the low-energy regime [3]. This fact had been theoretically predicted when it was shown that Dirac's field theory emerges [4,5] from Wallace's tight-binding model [6,7]. These characteristics of graphene allowed for establishing an analogy with relativistic quantum phenomena [8]. Even more so, it is possible to think of graphene as the mother of other graphitic materials since it can fold up to form fullerenes [9,10], roll up into carbon nanotubes [11], and stack up to shape graphite. Furthermore, using concepts from geometry and topology, carbon nanostructured curved materials can be created with unique properties [12,13]. Indeed, curved carbon materials were proposed more than a decade before the advent of groundbreaking graphene [14]. Although there is still no experimental synthesis of these nanostructured materials, there is a good expectation [15] that there will be so with technological advancement [13,16,17].

The possibility of studying quantum phenomena on curved space-times was also raised [18] with the logical implication to explore gravitational analogs phenomena in tabletop experiments [19,20], for instance, through the conformal-gauge symmetry encoded in the $2 + 1$ Dirac theory [21,22], the

intrinsic curvature of the graphene sheet gives up a general relativistic description of fermionic degrees of freedom, whereas the electronic properties of a sheet with a shape of a Beltrami trumpet [23] is interpreted as the Unruh-Hawking effect [24–26], forasmuch under a specific external magnetic field the space-time metric is described by a Zermelo optical metric which is conformally equivalent to the BTZ black hole metric [22], where also Hawking-radiation phenomena can be explored [27]. Likewise, using a variation of the hopping parameters in the tight-binding model, an emergent Horava gravity arises [28]. Additionally, a simulation of quantum gravity analogs can be achieved when chiral symmetry is broken; that is, when it considers trigonal warping of the electronic spectrum [29,30]. From the condensed matter perspective, the Dirac equation in the curved space is a natural model for studying the electronic properties of the graphene sheet when undulations [31–34] and topological defects are present; for instance, one can address the problem of impurities and topological defects [35,36]; in fact, the QFT formulation on the curved space might also describe the external strain acting on the material [37]. Furthermore, the corrugations on a curved sheet of graphene give up the appearance of a pseudomagnetic field [18,38], which is proportional to the Ricci scalar curvature [39,40].

Geometric and topology effects on the behavior of quantum states have been quite interesting to the community for a while. For example, by formulating Schr3dinger quantum mechanics on curves and surfaces using *confining potential formalism* [41–43], the quantum states are analyzed for

^{*}Corresponding author: pcastrov@unach.mx

particles confined to a helix, catenary, helicoid (or catenoid), and Möbius strip [44–47]. Also, evidence was found for reminiscences of an analogous quantum Hall effect when bending a strip helically [48,49]. At the same time, motivated by the physics behind a wormhole space-time in general relativity [50], the catenoid was shown to be the analogous wormhole model in $2+1$, while the external electric and magnetic background fields on the catenoid material give up bound states around the bridge and produce modified Landau levels [51]. From the intrinsic perspective, [52], a geometry-induced potential for Dirac fermions is deduced from the intrinsic geometry of the helicoid, resulting in the emergence of a pseudoelectric field near the potential minima giving rise to a chiral separation on the opposite rims of the helicoid [53].

The helicoid and catenoid are isometric surfaces belonging to the family of minimal surfaces, those surfaces that minimize area or, equivalently, those such that mean curvature is zero at each point on the surface, implying a negative Ricci scalar curvature. Also, minimal surfaces are solutions of the Willmore shape equation used to describe the conformation of soft surfaces in biophysics [54]. These surfaces were proposed three decades ago as representations of nanostructured allotropes of carbon obtained by decorating a minimal surface with carbon arrangement such as the triply periodic minimal surface by considering the inclusion of octagon rings in the carbon lattice structure [14]. Here, we assume that minimal surfaces are stable nanostructured graphitic shapes [12]; particularly, we focus on a subset of this family known as Bour surfaces [55] where the catenoid, helicoid, or the classical Enneper surface belong, among other surfaces, all characterized by their polar symmetry. As a consequence of the symmetry and the Weierstrass-Enneper (WE) representation [56], we can simplify the Dirac model in terms of two Dirac equations to study the electronic degrees of freedom in each of the valleys. Furthermore, we determine a geometry-induced potential for the Bour surface that generalizes that found for the helicoid [53]. In particular, we study the propagation of Dirac waves, in each valley, using the Lippmann-Schwinger (LS) equation along the latitudinal lines of the hypothesized material to address the problem of elucidating the role of geometry in the scattering states and the conductance of the material.

This paper is organized as follows. Section II introduces the noncoordinate basis notation and the WE representation for a minimal surface. These elements are necessary so that in Sec. III, we can write the Dirac equation in space-time $\mathbb{M} = \mathbb{R} \times \Sigma$, where Σ is a surface of Bour. In Sec. IV, the Dirac equation is rewritten so it can be interpreted as the equation for a Dirac fermion subjected to a repulsive potential coupled to a spin-orbit term. Furthermore, the asymptotic Dirac states are determined and used as initial states in Sec. V to determine the scattered states based on the LS formalism. Furthermore, in Sec. VI, the transmittance and reflectance coefficients are calculated using the Nöether current. In Sec. VII, conclusions and perspectives are presented; also, Appendices A–C have been added.

II. GEOMETRICAL PRELIMINARIES

This section introduces geometrical preliminaries suitable to set up the analysis of electronic degrees of freedom for

curved Dirac materials performed here. Particularly, it introduces the tetrad formalism for the geometry of a $2+1$ space-time, which allows us to write the Dirac equation on a curved space-time associated with the curved Dirac material. Additionally, the WE representation of a minimal surface, $\Sigma \subset \mathbb{R}^3$, is presented; it particularly introduces the Bour subfamily of minimal surfaces. These surfaces are introduced, since we shall analyze the electronic propagation on materials associated with the space-time $\mathbb{R} \times \Sigma$.

A. Tetrad formalism for a $2+1$ space-time

First, we introduce local coordinate bases for a $2+1$ space-time geometry \mathbb{M} . For the tangent space $T_p\mathbb{M}$, let the set $\{\partial_\mu\}$ be a local coordinate basis, whereas the set $\{dx^\mu\}$ the corresponding basis for the cotangent space $T_p^*\mathbb{M}$. Here, $p \in \mathbb{M}$ and the biorthogonality condition $dx^\mu(\partial_\nu) = \delta_\nu^\mu$ is satisfied. The Greek indices μ split in the chosen local coordinate patch.

The following presents a noncoordinate basis for the tangent space as the set $\{\hat{e}_A = e_\mu^A \partial_\mu\}$, where the capital Latin indices A are global indices $A = 0, 1, 2$, and the coefficients sort up in a matrix structure E , building up an element of $GL(3, \mathbb{R})$. These coefficients, called vielbeins, are attached to a local patch of the manifold \mathbb{M} . The noncoordinate basis is defined in such a way that it diagonalizes the metric tensor $g = g_{\mu\nu} dx^\mu \otimes dx^\nu$, that is, $g(\hat{e}_A, \hat{e}_B) = \eta_{AB}$, where $\eta_{AB} = \text{diag}(-1, 1, 1)$ is the Minkowski space-time metric. This means that one can write the metric tensor components as $g_{\mu\nu} = \eta_{AB} e_\mu^A e_\nu^B$, where e_μ^A are the elements of the inverse matrix E^{-1} . Additionally, the corresponding noncoordinate basis for the cotangent space is defined as the set $\{\hat{\theta}^A = e_\mu^A dx^\mu\}$. Now, the tensor metric can be written as $g = \eta_{AB} \hat{\theta}^A \otimes \hat{\theta}^B$, that is clearly diagonal. Remark that given a metric tensor g , the covectors $\hat{\theta}^A$ are not uniquely determined since there is a gauge freedom to choose $\hat{\theta}^A$ or $\Lambda_A^B \hat{\theta}^A$, where $\Lambda_A^B \in \text{SO}(2, 1)$ is a local element of the Lorentz group [57].

Now, let us introduce a connection one-form $\omega_B^A = \hat{\Gamma}_{CB}^A \hat{\theta}^C$, where $\hat{\Gamma}_{BC}^A$ are the coefficients of the affine connection, ∇ , defined through the equation $\nabla_A \hat{e}_B = \hat{\Gamma}_{AB}^C \hat{e}_C$. The connection one-form encodes geometrical information of \mathbb{M} through the Maurer-Cartan structure equations, which are given by

$$d\hat{\theta}^A + \omega_B^A \wedge \hat{\theta}^B = \mathcal{T}^A, \quad (1)$$

$$d\omega_B^A + \omega_C^A \wedge \omega_B^C = \mathcal{R}_B^A, \quad (2)$$

where \mathcal{T}^A and \mathcal{R}_B^A are the torsion and Riemann curvature of the manifold, respectively. Further, the connection one-form written in the local coordinate basis looks like $\omega^{AB} = \omega_\alpha^{AB} dx^\alpha$, where $\omega^{AB} = \eta^{BC} \omega_C^A$. Note that under a local Lorentz transformation, Λ , the connection one-form transform as $\omega_B^A = \Lambda_C^A \omega_D^C \Lambda_B^D + \Lambda_C^A \partial_\mu \Lambda_B^D$, where $\Lambda_B^D \equiv (\Lambda^{-1})_B^D$. Furthermore, if one asks for a Levi-Civita affine connection ∇ , one has the metric compatibility condition $\nabla_X g = 0$ for any vector field X . This implies the conditions $\omega_{AB} = -\omega_{BA}$ and $\mathcal{T}^A = 0$ [58].

B. Weierstrass-Enneper representation for a minimal surface, and Bour surfaces

Minimal surfaces are mathematical surfaces in the space corresponding to minimizing area surface or surfaces minimizing the Willmore energy [54]. The geometry of these surfaces is determined using the WE representation following Ref. [56]. The WE representation of a minimal surface can be cast in terms of the mapping $\mathbf{X} : \Omega \subset \mathbb{C} \rightarrow \Sigma \subset \mathbb{R}^3$ defined by

$$\mathbf{X}(\omega) = \mathbf{X}_0 + \text{Re} \int_{\omega_0}^{\omega} \Phi(\underline{\omega}) d\underline{\omega}, \quad (3)$$

with $\omega \in \Omega$, where Ω is a simply connected domain Ω . The differential volume $d\underline{\omega}$ represents an appropriate measure for Ω ; Re , and Im denote the real and imaginary parts, respectively. The function $\Phi(\omega)$ can be written in terms of a holomorphic function $\mathcal{F}(\omega)$ as

$$\Phi(\omega) = ((1 - \omega^2)\mathcal{F}(\omega), i(1 + \omega^2)\mathcal{F}(\omega), 2\omega\mathcal{F}(\omega)), \quad (4)$$

where $\mathcal{F}(\omega)$ is called Weierstrass function. The Gauss map using this WE representation is given by the normal vector field $\mathbf{N}(\omega) = (2\text{Re}\omega, 2\text{Im}\omega, |\omega|^2 - 1)/(1 + |\omega|^2)$. Additionally, by taking the real and imaginary parts of $\omega = u + iv \in \mathbb{C}$, respectively, it can be defined as a local patch with local coordinates $\{u, v\}$.

Given a specific Weierstrass function $\mathcal{F}(\omega)$, one can determine the parametrization $\mathbf{X}(\omega)$, which allows us to determine the whole extrinsic and intrinsic geometry of Σ . For instance, the main feature of a minimal surface is the vanishing mean curvature, $H = 0$. Furthermore, the intrinsic geometry of a minimal surface is described in terms of the metric tensor, introduced here, through the square of the line element $ds^2 = g_{ab}d\xi^a d\xi^b$, where the metric tensor components, g_{ab} , are calculated using the equation $g_{ab} = \partial_a \mathbf{X} \cdot \partial_b \mathbf{X}$, with indices $a, b = u, v$. Using the above parametrization of WE representation, it can be shown that $ds^2 = \Lambda^2(\omega)|d\omega|^2$, where $|d\omega|^2 = du^2 + dv^2$, and the conformal factor, $\Lambda^2(\omega)$, is given by $\Lambda^2(\omega) = |\mathcal{F}(\omega)|^2(1 + |\omega|^2)^2$. Thus, WE representation already gives local isothermal coordinates that always exist in a two-dimensional manifold [59]. In addition, the Gaussian curvature is given by $K = -4/|\mathcal{F}(\omega)|^2(1 + |\omega|^2)^4$ for points $\omega \in \Omega'$, where the set of regular points is given by $\Omega' = \{\omega \in \Omega : \mathcal{F}(\omega) \neq 0\}$. In the following, we focus on a subfamily of minimal surfaces known as Bour's minimal surfaces [55,56] defined through the Weierstrass function $\mathcal{F}(\omega) = c\omega^{n-2}$, where $c \in \mathbb{C}$ and $n \in \mathbb{R}$. In this subfamily belong the catenoid with $n = 0$ and $c = R_0/2$, R_0 being the radius of the neck; the helicoid with $n = 0$ and $c = i\alpha$, α being the pitch of the helicoid, and the Enneper surface with $n = 2$, $c = 1$. Also, it is known that n and $-n$ represent the same Bour surface; thus, it is enough to consider the cases $n \geq 0$ [55]. Notice that in the case of the Bour's surfaces, the conformal factor depends just on the norm $|\omega| = \sqrt{u^2 + v^2}$, thus it is convenient to use polar coordinates, (r, θ) , defined as usual, $r = |\omega|$ and $\theta = \arctan(v/u)$. The conformal factor is just given by

$$\Lambda(r) = |c|r^{n-2}(1 + r^2), \quad (5)$$

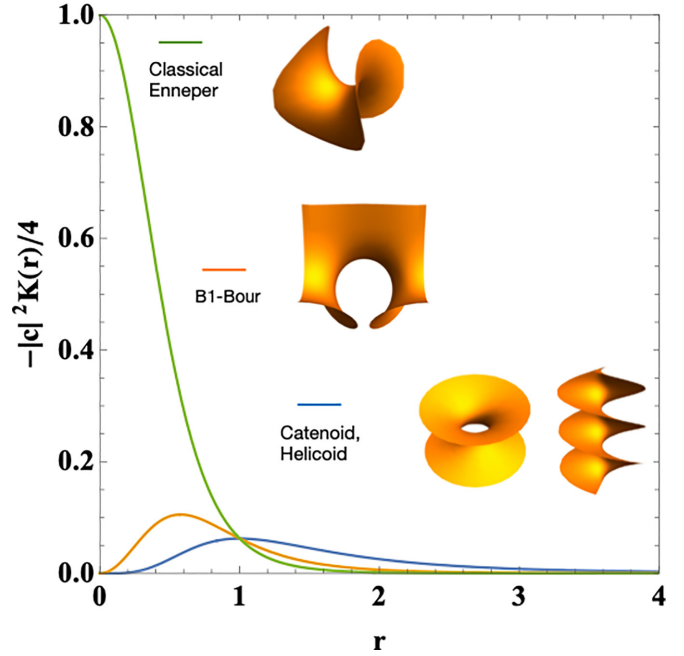


FIG. 1. Negative of Gaussian curvature [Eq. (6)] vs radial coordinate r for the cases $n = 0, 1, 2$. The figure also shows examples of minimal Bour surfaces from top to bottom: classical Enneper, B_1 -Bour, catenoid, and helicoid surfaces, respectively. All the surfaces inset have a finite value of curvature.

where we recall $c \in \mathbb{C}$ and $n \geq 0$ are parameters that give a specific Bour's surface. Now, the Gaussian curvature of these surfaces is given by

$$K(r) = -\frac{4}{|c|^2 r^{2(n-2)}(1 + r^2)^4}. \quad (6)$$

By inspection, one can see that the Gaussian curvature is finite for $r \in \mathbb{R}$ for the cases $n = 0, 1, 2$ [see Fig. 1], while for $n > 2$ all the B_n -Bour surfaces have a singular curvature at $r = 0$. In addition, since Gaussian curvature has units of the inverse square of the length $|c|$, it gives a natural length unit for a Bour surface. Note that the catenoid and helicoid have the same Gaussian curvature since these surfaces are isometric. In addition, denoting $dA = \sqrt{g}drd\theta$ the area element, let us note that the total curvature of each Bour surface Σ has the same value, that is, $\int_{\Sigma} dA K = -4\pi$; however, this does not mean that they have the same topology, for instance, the Enneper surface is simply connected but catenoid is not [60].

III. DIRAC FIELD ON THE CURVED SPACE-TIME $\mathbb{M} = \mathbb{R} \times \Sigma$

This section introduces the Dirac model on a space-time geometry with the global structure $\mathbb{M} = \mathbb{R} \times \Sigma$, where Σ is a minimal surface. Later, Σ is specified as a specific member of the Bour minimal surface family.

A. Dirac model with an artificial SU(2) gauge field on the material curved space-time

The starting point is the Dirac equation $i\underline{\gamma}^\alpha \nabla_\alpha \psi = 0$, defined on a 2 + 1 space-time \mathbb{M} , where $\underline{\gamma}^\alpha(x) = \gamma^A e_A^\alpha(x)$ for

$x \in \mathbb{M}$, where e_A^α are the vielbeins introduced in the previous section and γ^A being the Dirac matrices that satisfy the Clifford algebra

$$\{\gamma^A, \gamma^B\} = 2\eta^{AB}\mathbb{1}, \quad (7)$$

where γ^A have range 2 and $\mathbb{1}$ is the unit diagonal matrix. A suitable representation of the Dirac matrices in $2+1$ space-time dimension that satisfy the Clifford algebra Eq. (7) is given by the matrices $\gamma^0 = -i\sigma_3$, $\gamma^1\gamma^0 = \sigma_1$ and $\gamma^2\gamma^0 = \sigma_2$, where σ_i , are the standard Pauli matrices, with $i = 1, 2, 3$. In addition, ∇_α are the covariant derivative for the spinor representation of the Lorentz group $SO(2, 1)$ acting on the Dirac spinors as $\nabla_\alpha\psi$, where $\nabla_\alpha = \partial_\alpha + \Omega_\alpha$, $\Omega_\alpha = \frac{1}{8}\omega_\alpha^{AB}[\gamma_A, \gamma_B]$ being the spin connection, and ω_α^{AB} are the components of the Maurer-Cartan one-form connection defined in the previous section.

To introduce the Dirac model on the curved material, let us remark that on the curved sheet of graphene, two Dirac fields are presented, Ψ_\uparrow and Ψ_\downarrow , in a $SU(2)$ color doublet

$$\chi = \begin{pmatrix} \Psi_\uparrow \\ \Psi_\downarrow \end{pmatrix} \quad (8)$$

to consider valley degrees of freedom. Dirac spinors Ψ_\uparrow and Ψ_\downarrow contribute equally whenever the valley symmetry has not been broken. Thus, strictly speaking, the propagation of the electronic degrees of freedom is given by

$$i\Gamma^\mu\nabla_\mu\chi = 0, \quad (9)$$

where the Dirac matrices now are $\Gamma^\mu = \gamma^\mu \otimes \mathbb{1}$, and the spinorial covariant derivative $\nabla_\mu = \mathbb{1} \otimes \mathbb{1}\partial_\mu + \Omega_\mu \otimes \mathbb{1}$ [61]. Furthermore, for the nanostructured material to preserve the topology of a minimal surface, it is necessary to insert heptagonal rings [14]; this is because this class of surfaces has negative Gaussian curvature at each point. Although our work does not contemplate an analysis at the lattice level, as does the tight-binding model, it is known that such intrusions are considered topological defects, which modify the energy spectrum and the number of states [62].

At the level of the continuous model, the topological defects manifest as non-Abelian magnetic fluxes that go out transversally to the surface through the heptagonal incisions [18,35,63,64]. Thus, we ask whether this non-Abelian gauge field influences the Nöether current used below for the transmittance analysis. The Dirac field coupled with a non-Abelian gauge field is considered to answer this question,

$$i\Gamma^\mu(\nabla_\mu - i\mathbb{A}_\mu)\chi = 0, \quad (10)$$

where \mathbb{A}_μ is the non-Abelian gauge field taking values in the Lie algebra of $SU(2)$, which strictly must be written as $\mathbb{1} \otimes \mathbb{A}_\mu$, and χ turns out to be a $SU(2)$ color doublet that contains the two-component of the Dirac spinor mentioned above. In the continuum limit, we consider the approximation that the field is zero in the neighborhood of a finite flux traversing a section with effective area zero, thus the artificial non-Abelian gauge field is considered as a pure gauge field [64]

$$\mathbb{A}_\mu(x) = iU^{-1}(x)\partial_\mu U(x), \quad (11)$$

where $U(x)$ is a local element of the group $SU(2)$. Note that the strength tensor $\mathbb{F}_{\mu\nu} = \nabla_\mu\mathbb{A}_\nu - \nabla_\nu\mathbb{A}_\mu - i[\mathbb{A}_\mu, \mathbb{A}_\nu]$ is locally zero for the gauge field Eq. (11), but the flux is different

than zero to take into account the topological defects. Next, we choose a coordinate chart and specific gauge field to approach this problem.

B. Polar coordinates and the gauge field on $\mathbb{M} = \mathbb{R} \times \Sigma$

The metric of the space-time $\mathbb{R} \times \Sigma$ using polar coordinates is written through the square of the line element as follows:

$$ds^2 = -v_F^2 dt^2 + \Lambda^2(r, \theta)(dr^2 + r^2 d\theta^2). \quad (12)$$

The local indices, in this case, can be split as $\alpha = t, r, \theta$. From the metric Eq. (12), one can easily read $\hat{\theta}^0 = v_F dt$, $\hat{\theta}^1 = \Lambda dr$ and $\hat{\theta}^2 = \Lambda r d\theta$, from where one can extract the components of the vielbeins e_μ^A [65]. Also, recall that once $\hat{\theta}^A$ have been chosen, the gauge associated with the Lorentz invariance is fixed. Now, from the Maurer-Cartan Eq. (1) and the torsionless condition, one can obtain $d\hat{\theta}^0 = 0$, and

$$d\hat{\theta}^1 + \frac{\Lambda_\theta}{\Lambda^2 r} \hat{\theta}^1 \wedge \hat{\theta}^2 = 0, \quad (13)$$

$$d\hat{\theta}^2 + \frac{(\Lambda r)_r}{\Lambda^2 r} \hat{\theta}^2 \wedge \hat{\theta}^1 = 0, \quad (14)$$

where $(X)_r \equiv \partial_r X$. Now, from Eq. (13) one can deduce $\omega_0^1 = 0$ and $\omega_2^1 = \frac{\Lambda_\theta}{\Lambda^2 r} \hat{\theta}^1 + X \hat{\theta}^2$ for some local function X , whereas from Eq. (14) one can deduce that $\omega_0^2 = 0$ and $\omega_1^2 = \frac{(\Lambda r)_r}{\Lambda^2 r} \hat{\theta}^2 + \tilde{X} \hat{\theta}^1$. Now, we use the metric condition, $\omega^{AB} = -\omega^{BA}$, thus one can determine X and \tilde{X} , turning that the only nonzero components of the connection one-form are

$$\omega^{12} = -\omega^{21} = \frac{\Lambda_\theta}{\Lambda^2 r} \hat{\theta}^1 - \frac{(\Lambda r)_r}{\Lambda^2 r} \hat{\theta}^2. \quad (15)$$

These components expressed in local coordinates are given by $\omega_r^{12} = -\omega_r^{21} = \frac{1}{r} \partial_\theta \log \Lambda$ and $\omega_\theta^{12} = -\omega_\theta^{21} = -\frac{1}{\Lambda} \partial_r (\Lambda r)$. Consequently, the spin connection Ω_α is given simply by $\Omega_t = 0$, $\Omega_r = \frac{i}{2} \frac{1}{r} \partial_\theta (\log \Lambda) \sigma_3$, and $\Omega_\theta = -\frac{i}{2} \frac{1}{\Lambda} \partial_r (\Lambda r) \sigma_3$.

The above coordinates (r, θ) are particularly useful for the Dirac model since the conformal factor Λ for the Bour's minimal surface family depends just on the coordinate r . In this case, due to the polar symmetry, the non-Abelian gauge field must be of the form $\mathbb{A}_\theta = \frac{\varphi}{2\pi} \tau_2$, $\mathbb{A}_t = \mathbb{A}_r = 0$, as suggested in Refs. [62,63], where τ_2 is the second Pauli matrix in the space of the two Dirac points. This field can be written like the previous expression Eq. (11) using the group element $U = e^{-i\theta \frac{\varphi}{2\pi} \tau_2}$.

Now we use all this information to write an explicit expression for the Dirac Eq. (10) in polar coordinates. Denoting the $2+1$ doublet Dirac spinor by χ and now performing the transformation $\chi = r^{-\frac{1}{2}} \Lambda^{-\frac{1}{2}} \Phi$, we can show that the Dirac equation can be written as

$$i\hbar\partial_t\Phi = -i\frac{\hbar v_F}{\Lambda} \left(\sigma_1 \partial_r \Phi + \frac{1}{r} \sigma_2 \left(\partial_\theta - i\frac{\varphi}{2\pi} \tau_2 \right) \Phi \right). \quad (16)$$

Following the same strategy as Ref. [63], i.e., by passing to the basis of eigenvectors of τ_2 , the above equation can be written

as the two Dirac equations

$$i\hbar\partial_t\Phi^\tau = -i\frac{\hbar v_F}{\Lambda}\left(\sigma_1\partial_r\Phi^\tau + \frac{1}{r}\sigma_2\left(\partial_\theta - i\frac{\tau\varphi}{2\pi}\right)\Phi^\tau\right), \quad (17)$$

where $\tau = \pm$ is the valley index and the eigenvalues of τ_2 . As we can appreciate in Eq. (17), the topological defects are taken into account by introducing an effective non-Abelian gauge flux φ in two Dirac equations. Since, in the present paper, we lack specific lattice geometry, one cannot infer a value for the artificial flux φ as it is performed in previous works [62,63]. However, according to Ref. [64], the value of each individual flux is classified in two forms $\pm\frac{\pi}{2}$ and $\pm\frac{\pi}{6}$, depending on the disposition of the defects in the lattice; if one has N heptagons intrusions, the value of the effective fluxes in each case correspond to $\frac{\varphi}{2\pi} = \pm\frac{N}{4}$ and $\frac{\varphi}{2\pi} = \pm\frac{N}{12}$. Since the lattice geometry of Bour surfaces is presently unknown, we will utilize these values as working examples for the time being and defer the construction of particular lattices to future research.

IV. GEOMETRY-INDUCED POTENTIAL AND ASYMPTOTIC STATES ON THE BOUR'S MINIMAL SURFACES FAMILY

This section determines the geometry-induced potential and the Dirac asymptotic states on the Bour's minimal surface. These states are defined as the solutions of the Dirac equation for $r \rightarrow \infty$.

A. Dirac fermions under effective potential

Our starting point is the Dirac equation on polar coordinates deduced above Eq. (17), where the conformal factor $\Lambda(r)$ is given just by Eq. (5). Since the conformal factor depends on just one of the coordinates, one can make a further change of variables using the transformation

$$x_n(r) = \int \Lambda(r)dr = |c|\left[\frac{r^{n-1}}{n-1} + \frac{r^{n+1}}{n+1}\right] \quad (18)$$

for $n \neq 1$, while for $n = 1$ the appropriate change of variable is $x_1(r) = |c|(\log r + \frac{1}{2}r^2)$. One can verify that these transformations are injective maps; thus, one can guarantee the existence of their corresponding inverse functions $r = r(x)$, where x would be defined in an appropriate domain \mathcal{D}_x . Using this variable, each Dirac equation from Eq. (17) can be simplified as

$$i\hbar\partial_t\Phi^\tau = v_F\sigma_1\hat{p}_x\Phi^\tau + v_F\sigma_2V(x)\hat{J}_{\theta,\tau}\Phi^\tau, \quad (19)$$

where $\hat{p}_x = -i\hbar\partial_x$ is a linear momentum operator and $\hat{J}_{\theta,\tau} = \hat{\ell}_\theta + \frac{\tau\varphi}{2\pi}\hbar$ is a total angular momentum, being $\hat{\ell}_\theta = -i\hbar\partial_\theta$ the two-dimensional angular momentum operator and $\tau\frac{\varphi}{2\pi}\hbar$ a valley pseudospin. Noticeably, the second term of this equation can be interpreted as an effective potential; although this term comes entirely from the intrinsic geometry of the surface, this potential is geometry induced. The effective potential is given by

$$V(x) = \frac{1}{r(x)\Lambda(r(x))}. \quad (20)$$

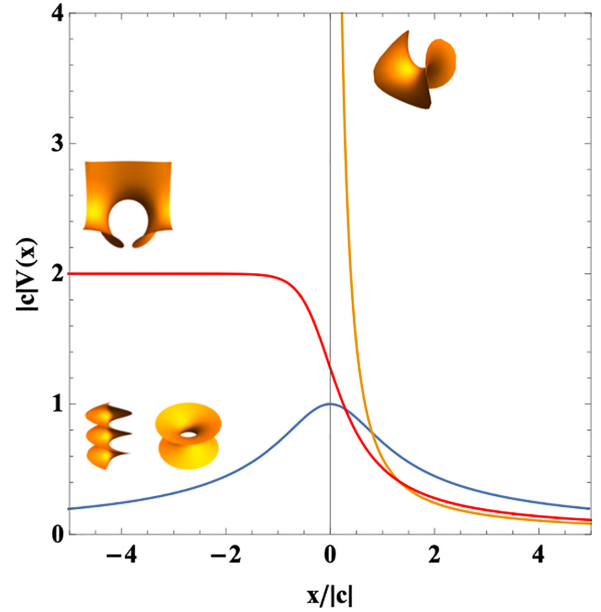


FIG. 2. Effective potential [Eq. (20)] vs coordinate x Eq. (18) for the classical Enneper ($n = 2$), B_1 -Bour, $n = 1$, and catenoid (helicoid) ($n = 0$).

This potential generalizes the effective potential found in Ref. [53] for the helicoid.

Let us note that for those cases with $n \geq 2$, such as the classical Enneper surface, the domain of the variable x is \mathbb{R}^+ [see Eq. (18)]. Thus, it is useful to define an extension to the whole reals defining $U(x) = V(x)$ for $x \geq 0$ and $U(x) = V(-x)$ for $x \leq 0$ as an extension for $x \in \mathbb{R}$. This construction makes the potential symmetric, and the Dirac equation for this extension turns out to be $i\hbar\partial_t\Phi^\tau = v_F\sigma_1\hat{p}_x\Phi^\tau + v_F\sigma_2U(x)\hat{J}_{\theta,\tau}\Phi^\tau$, which reduces to Eq. (19) for $x \geq 0$.

Now, we deduce the main characteristics of the effective potential $V(x)$. Using the conformal factor Eq. (5) and the change of variable $x(r)$, it can be shown that near $x \approx 0$ for the catenoid (or helicoid) surface with $n = 0$, the potential is $V(x) \approx c$, where c is a positive constant; for B_1 -Bour surface $n = 1$, the potential is linear $V(x) \simeq mx + b$, with a negative slope m and a positive y -intercept b ; and for any Bour surface with $n > 1$, the effective potential behaves as $V(x) = c/((n-1)x)$ for some positive constant c . Therefore, the potential $V(x)$ is a scattering potential. Furthermore, we are interested in the states far away from the center $x = 0$ to use them as initial states propagating along the surface. Additionally, one can verify that the effective potential, $V(x)$, vanishes for $x \rightarrow \infty$ for all $n \geq 0$. Figure 2 plots the geometry-induced potential for the first three cases $n = 0, 1, 2$.

a. Example B_0 (catenoid/helicoid). Let us note that, for example, in the case of the catenoid (or helicoid) $n = 0$ and $|c| = R_0/2$, one has $x = \frac{R_0}{2}(r - r^{-1})$, where the domain is the whole \mathbb{R} and recall R_0 is the radius of the neck of the catenoid. Using the expression for the conformal factor Eq. (5) and the generalized effective potential Eq. (20), it is straightforward to show that $V(x) = 1/\sqrt{x^2 + R_0^2}$, which satisfies the qualitative characteristics deduced above. Note that this effective potential is the same found in Ref. [53].

b. Example (B_1 -Bour surface). Let us note that, for example, in the case of B_1 -Bour surface $n = 1$ and choosing $c = 1$, one has $x = \log r + \frac{1}{2}r^2$, where the domain is the whole \mathbb{R} . One can express r in terms of x using the principal value of the Lambert W function $r^2 = W(e^{2x})$. Using the expression for the conformal factor Eq. (5) and the generalized effective potential Eq. (20), it is straightforward to show that $V(x) = 1/(1 + W(e^{2x}))$, which satisfies the qualitative characteristics deduced above.

c. Example B_2 (Enneper surface). Now, for the Enneper classical surface $n = 2$ using $c = 1$, one has

$$x = r + \frac{r^3}{3}. \quad (21)$$

Let us note that contrary to the previous examples, in this case, the domain of this variable $x \in \mathbb{R}^+$. Using the expression for the conformal factor Eq. (5) and the generalized effective potential Eq. (20) is $V(x) = 1/(r(x) + r^3(x))$, thus one needs to find the positive root of a third-order polynomial Eq. (21). The effective potential in terms of x is given explicitly by

$$V(x) = \frac{1}{3x + 2^{\frac{2}{3}}(R_-^{\frac{1}{3}}(x) - R_+^{\frac{1}{3}}(x))}, \quad (22)$$

where $R_{\pm}(x) = \sqrt{9x^2 + 4} \pm 3x$. Note that series expansion of $R_{\pm}^{\frac{1}{3}}(x)$ around $x \simeq 0$ is $R_{\pm}^{\frac{1}{3}}(x) \simeq 2^{\frac{1}{3}} \pm 2^{-\frac{2}{3}}x$. Thus, the effective potential near $x = 0$ behaves similarly to a Coulombic-type potential, $V(x) \simeq \frac{1}{x}$, while it is clear that for large values of x , that is for $x \rightarrow \infty$ the potential $V(x)$ vanishes as was shown qualitatively above.

B. Qualitative analysis of quantum states

An alternative way to qualitatively understand the nature of the states consists of decoupling Eq. (19) into two Schrödinger-type equations as was done for the helicoid case in Ref. [53]. Indeed, by squaring the operators on each side of Eq. (19), it is not so difficult to obtain

$$-\hbar^2 \partial_t^2 \Phi = v_F^2 (\hat{p}_x^2 + \hat{J}_\theta^2 V^2(x) + \sigma_3 \hbar \hat{J}_\theta V'(x)) \Phi, \quad (23)$$

where we are ignoring the notation \pm for the sake of simplicity and $V'(x) = \frac{d}{dx} V(x)$.

Now, writing the stationary states in the form $\Phi = e^{i\frac{Et}{\hbar} + im\theta} U(x)$, it is straightforward to obtain the time-independent Schrödinger-type equation

$$\left[-\frac{d^2}{dx^2} + V_{\text{eff}}^{m,\alpha}(x) \right] U_\alpha(x) = \epsilon U_\alpha(x) \quad (24)$$

for each spinorial component $U_\alpha(x)$ with $\alpha = \pm$ for the upper and lower spinorial components, respectively, where

$$V_{\text{eff}}^{m,\alpha}(x) = m_\tau^2 V^2(x) + \alpha m_\tau V'(x), \quad (25)$$

with $m_\tau = m + \frac{\tau\varphi}{2\pi}$ and $\epsilon = (E/(\hbar v_F))^2$. Let us first note that this potential vanishes for those cases when $m_\tau = 0$; this happens when quantum number m turns out to be $m = \frac{\varphi}{2\pi}$ or $m = -\frac{\varphi}{2\pi}$; this case describes the propagation of a Dirac wave in one valley without obstacles, while the Dirac wave in the other valley encounters some resistance.

The potential Eq. (25) is the same obtained in the study of a helical nanoribbon performed in Ref. [53] when we

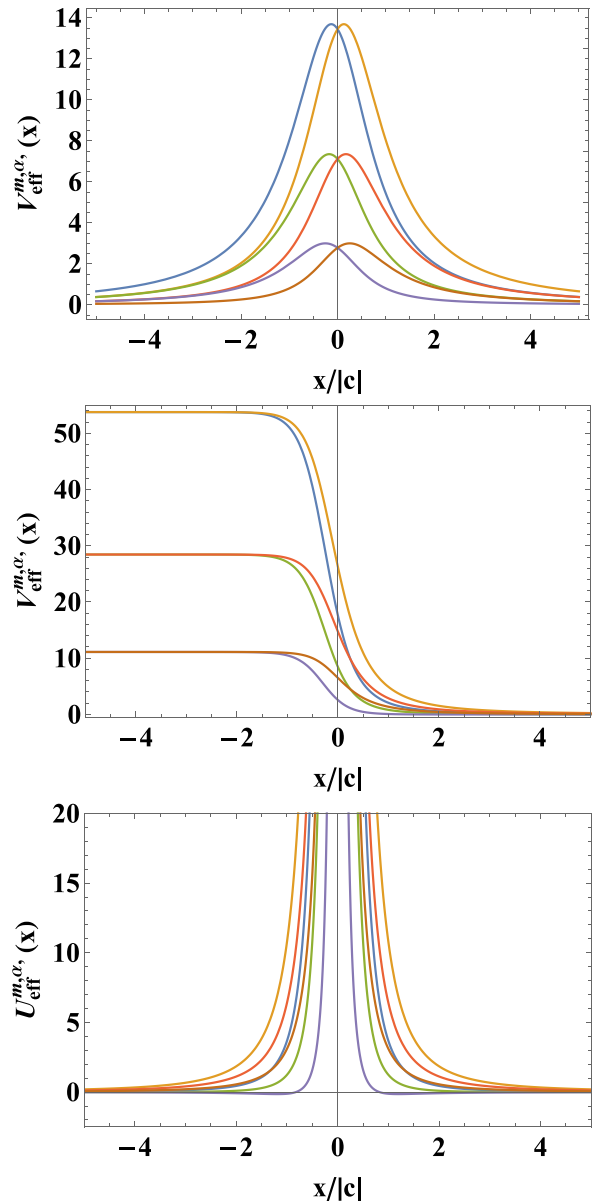


FIG. 3. Effective potential [Eq. (25)] vs coordinate x . Top for the catenoid (helicoid) ($n = 0$), middle for the B_1 -Bour surface, $n = 1$, and down for the classical Enneper ($n = 2$). Each effective potential is plotted for each case $m \in \{-1, 0, 1\}$, $\alpha = \pm$ with an effective gauge flux $\frac{\varphi}{2\pi} = 8/3$.

substitute $V(x)$ in the case of the catenoid (example B_0 above) and take zero topological flux $\varphi = 0$; this means that similar conclusions obtained in Ref. [53] are obtained in the case of the catenoid, at least near the catenoid neck. In Fig. 3, we present the behavior of $V_{\text{eff}}^{m,\alpha}(x)$ for the catenoid, B_1 -Bour, and Enneper surface for the working example of a flux $\frac{\varphi}{2\pi} = \frac{N}{12} = 8/3$. For the catenoid surface and B_1 -Bour, the potential for each m is similar to a potential barrier. In contrast, in the case of Enneper, the potential is a potential barrier except for the cases $m = 1$, where there is a region where bound states could exist. However, note that this region is required for $\epsilon < 0$, which means that E is imaginary, so we associate these states with quasibound states. Remark that the structure of the effective potential

$V_{\text{eff}}^{m,\alpha}(x)$ does not change qualitatively from other values of the flux φ .

C. Asymptotic Dirac states on the Bour's minimal surfaces

The previous analysis allows us to justify that for the asymptotic states, the second term of Eq. (19) can be neglected. Thus, the equation reduces to a $1+1$ -Dirac equation $i\partial_t \Phi^\tau = v_F \sigma_1 \hat{p}_x \Phi^\tau$. For the solutions of this equation, we propose the spinor solution as $\Phi^\tau(x, \theta, t) = e^{ikx - i\frac{Et}{\hbar}} f(\theta)v$, where the function $f(\theta)$ is an arbitrary nonzero periodic function in the azimuthal angle θ , and v is a vector that acquires the pseudospin character of the spinor. These solutions are independent of the valley index τ . By imposing the one-dimensional Dirac equation, the dispersion relation turns out to be $E = \pm \hbar v_F |k|$, and v satisfies the equation $\hat{h}v = \pm \frac{1}{2}v$, where \pm refers to a positive and energy Dirac states, where

$$\hat{h} = \frac{1}{2} \sigma_1 \frac{k}{|k|} \quad (26)$$

is the one-dimensional analog of the helicity operator. For positive energy value, the pseudospin states are given by v_\uparrow (v_\downarrow) for positive (negative) helicity $k > 0$ ($k < 0$), whereas for negative energy values the pseudospin states are interchanged themselves, $v_\uparrow \rightarrow v_\downarrow$, where the normalized states $\{v_\uparrow, v_\downarrow\}$ are given by

$$v_\uparrow = \frac{1}{\sqrt{2}} \begin{pmatrix} 1 \\ 1 \end{pmatrix} \quad \text{and} \quad v_\downarrow = \frac{1}{\sqrt{2}} \begin{pmatrix} 1 \\ -1 \end{pmatrix}. \quad (27)$$

For positive energy values, one has the following two independent solutions: $\Phi_{+,+}(x, \theta, t) = e^{ikx - i\frac{Et}{\hbar}} f(\theta)v_\uparrow$ and $\Phi_{+,-}(x, \theta, t) = e^{ikx - i\frac{Et}{\hbar}} f(\theta)v_\downarrow$ for positive and negative helicity, $k > 0$ and $k < 0$, respectively. Similarly, for negative values of energy, one has $\Phi_{-,+}(x, \theta, t) = e^{ikx + i\frac{Et}{\hbar}} f(\theta)v_\downarrow$ and $\Phi_{-,-}(x, \theta, t) = e^{ikx + i\frac{Et}{\hbar}} f(\theta)v_\uparrow$ for positive and negative helicity, $k > 0$ and $k < 0$, respectively. These four states can be cast together as follows: $\Phi_{\mu,\sigma}^\tau(x, \theta, t) = \Phi_{\mu,\sigma}(x, \theta) e^{-i\mu\frac{Et}{\hbar}}$, being

$$\Phi_{\mu,\sigma}(x, \theta) = e^{i\sigma|k|x} f(\theta)v_{\mu,\sigma}, \quad (28)$$

where we have introduced a mnemonic rule for $\mu \cdot \sigma$ as $+\cdot+ = \uparrow$, $-\cdot+ = \downarrow$, $+\cdot- = \downarrow$ and $-\cdot- = \uparrow$, where $\mu = \text{sgn}(E)$. Finally, let us recall that the transformation performed above, $\Psi = \Phi/\sqrt{r\Lambda}$, thus the asymptotic Dirac state far away from the scattered center is given by

$$\Psi_{\mu,\sigma}^\tau(x, \theta, t) = \sqrt{V(x)} e^{i\sigma|k|x - i\mu\frac{Et}{\hbar}} f(\theta)v_{\mu,\sigma}, \quad (29)$$

which vanishes for $x \rightarrow \infty$. In addition, as a consequence of the periodicity of the function $f(\theta) = f(\theta + 2\pi)$, one can write the following series representation: $f(\theta) = \sum_{m \in \mathbb{Z}} f_m e^{im\theta}$.

V. SCATTERING ANALOG ON THE BOUR'S SURFACES

A. Outscattering states by Lippmann-Schwinger equation

In this section, we introduce the LS equation [66,67] to study how the states propagate along the surface considered. In particular, we are interested in describing the manner in

which the initial states, found above, are scattered due to the effective potential $V(x)$. Let us consider the Hamiltonian $\hat{H} = \hat{H}_0 + \hat{V}$ split between a free Hamiltonian \hat{H}_0 and a perturbed potential \hat{V} . Now, the LS equation is given by

$$|\Phi\rangle = |\Phi_{\text{in}}\rangle + \frac{1}{E - \hat{H}_0 + i\epsilon} \hat{V} |\Phi\rangle, \quad (30)$$

where $|\Phi_{\text{in}}\rangle$ is the initial state and $|\Phi\rangle$ is the out scattering state. Note that, in general, we are considering that \hat{H}_0 and \hat{V} are differential matrix operators acting on spinors. Thus, the states $\{|\Phi\rangle\}$ acquire spinorial components.

The Born approximation is obtained by substituting $|\Phi_{\text{in}}\rangle$ instead of $|\Phi\rangle$ in the second term of the LS Eq. (30). To go further to higher-order approximation, it is standard to introduce the transition operator \hat{T} defined using the equation $\hat{T}|\Phi_{\text{in}}\rangle = \hat{V}|\Phi\rangle$. In fact, multiplying the LS equation by \hat{V} , one arrives at the well-known self-consistent recursive operator equation for the transition operator \hat{T} :

$$\hat{T} = \hat{V} + \hat{V} \frac{1}{E - \hat{H}_0 + i\epsilon} \hat{T}. \quad (31)$$

A series solution for \hat{T} can be gotten using this equation through a usual iterative procedure

$$\hat{T} = \hat{V} + \hat{V} \frac{1}{E - \hat{H}_0 + i\epsilon} \hat{V} + \hat{V} \frac{1}{E - \hat{H}_0 + i\epsilon} \hat{V} \frac{1}{E - \hat{H}_0 + i\epsilon} \hat{V} + \dots, \quad (32)$$

where the first approximation $\hat{T} \simeq \hat{V}$ corresponds to the so-called Born approximation.

To determine the out scattering states, one can follow two common procedures that are to project $\{|\Phi\rangle\}$ along space states $\{|\mathbf{x}\rangle\}$ or momentum states $\{|\mathbf{p}\rangle\}$. For the projection along the space states, one obtains the spinorial wave function $\Psi(\mathbf{x}) = \langle \mathbf{x} | \Phi \rangle$, where $\mathbf{x} = (x_1, x_2)$ are certain coordinates associated with a local patch on the surface. Thus, using the transition operator, the LS equation can be rewritten as

$$\Phi(\mathbf{x}) = \Phi_{\text{in}}(\mathbf{x}) + \int_{\mathcal{D}} d^2\mathbf{x}' \mathbb{G}(\mathbf{x}, \mathbf{x}') \langle \mathbf{x}' | \hat{T} | \Phi_{\text{in}} \rangle, \quad (33)$$

where the Green's function satisfies the Green's equation defined by

$$(E - \hat{H}_0) \mathbb{G}(\mathbf{x}, \mathbf{x}') = \mathbb{1} \delta(\mathbf{x} - \mathbf{x}'). \quad (34)$$

Now, when we project the outscattering states along the momentum states, one obtains the spinorial wave function in the momentum space, which we have abusively written with the same notation $\Phi(\mathbf{p}) = \langle \mathbf{p} | \Phi \rangle$. Assuming that \hat{H}_0 is an operator that depends exclusively on the momentum operator, thus the LS equation can be written as

$$\Phi(\mathbf{p}) = \Phi_{\text{in}}(\mathbf{p}) + \frac{1}{E - H_0(\mathbf{p}) + i\epsilon} \langle \mathbf{p} | \hat{T} | \Phi_{\text{in}} \rangle, \quad (35)$$

where $H_0(\mathbf{p})$ is the matrix free Hamiltonian evaluated at the momentum value \mathbf{p} .

B. Out scattering states on the Bour surfaces

In this section, we study the electronic states on the Bour surfaces starting from Eq. (19). Noticeably, the second term

of this equation can be thought of as a barrier potential. This potential energy is crucial in the behavior of the Dirac particle states on the Bour surface. Now, to implement the LS Eq. (30) we identify the free Hamiltonian $\hat{H}_0 = v_F \sigma_1 \hat{p}_x$ and the perturbed Hamiltonian by $\hat{V} = v_F \sigma_2 U(x) \hat{J}_{\theta, \tau}$, where we recall $U(x)$ as the symmetrized form of the effective potential $V(x)$. In the following, we carry out the Born and higher-order Born approximations to determine the outscattering states on the curved surface.

1. Born approximation

Now, to determine the outscattering states $\Psi(\mathbf{x})$, we consider the initial states $\Phi_{\text{in}, \sigma}(x)$ far away from the scattering center, which in our case correspond to $x \simeq 0$. In particular, the states that are considered here are $\Phi_{\text{in}}(\mathbf{x}) = \Phi_{\mu, \sigma}(x, \theta)$ found in the last section [see states given by Eq. (28)]. Since the free Hamiltonian \hat{H}_0 is independent of θ , thus the Green's function acquires the expression $\mathbb{G}(\mathbf{x}, \mathbf{x}'; E) = \mathbb{G}(x - x'; E) \delta(\theta - \theta')$, where $\mathbf{x} = (x, \theta)$. Now, the LS equation, in this case, can be written as

$$\begin{aligned} \Phi^\tau(x, \theta) &= \Phi_{\text{in}}(x, \theta) \\ &+ v_F \int_{-\infty}^{\infty} dx' \mathbb{G}(x - x'; E) U(x') \sigma_2 \hat{J}_{\theta, \tau} \Phi^\tau(x', \theta), \end{aligned} \quad (36)$$

where $\mathbb{G}(x - x'; E)$ is the Green's function for the one-dimensional operator $E - v_F \sigma_1 \hat{p}_x$, that is, a function that satisfies $(E - v_F \sigma_1 \hat{p}_x) \mathbb{G}(x - x'; E) = \delta(x - x') \mathbb{1}$. Following the standard procedure (see Appendix A), it is not difficult to show that

$$\mathbb{G}(x - x'; E) = \frac{1}{2i\hbar v_F} [\text{sgn}(E) + \text{sgn}(x - x') \sigma_1] e^{i \frac{|E|}{\hbar v_F} |x - x'|}, \quad (37)$$

where we recall that $E = \pm \hbar v_F |k|$. In the following, as a consequence of the polar geometry of the surface, the states $\Phi^\tau(x, \theta)$ are periodic in the angular variable θ . Thus, it can be written in the next expansion $\Phi^\tau(x, \theta) = \sum_{m \in \mathbb{Z}} \Phi_m(x) e^{im\theta}$. Now, using the orthonormal relation of the basis $\{e^{im\theta}\}$ one has the following integral equation for $\Phi_m^{(\mu)}(x)$, that is:

$$\begin{aligned} \Phi_m^{\tau(\mu)}(x) &= e^{i\sigma|k|x} f_m v_{\mu, \sigma} \\ &+ \hbar v_F m_\tau \int_{-\infty}^{\infty} dx' \mathbb{G}(x - x'; E) U(x') \sigma_2 \Phi_m^{\tau(\mu)}(x'), \end{aligned} \quad (38)$$

where we have introduced the labeled μ to distinguish the positive and energy outscattering states; also recall that $\mu = \text{sgn}(E)$. At the Born approximation, it is enough to make the substitution $\Phi_m^{(\mu)}(x')$ by $e^{i\sigma p x'} f_m v_{\mu, \sigma}$ in the second term of the last equation, where we have defined the magnitude of the momentum $|k| = p$. Let us choose an initial wave with $\sigma = -$, that is, a left wave with $k < 0$ going to the scattering center. Noticeably, after a straightforward calculation, the states are given by

$$\Phi_m^{\tau(\mu)}(x) \simeq f_m [e^{-ipx} v_{-\mu} + m_\tau \tilde{U}(2p) e^{ipx} v_\mu], \quad (39)$$

where we have found that negative energy states with pseudospin up \uparrow propagating along the scattering center reflecting into a pseudospin down \downarrow . The amplitude of the reflection is given by $m_\tau \tilde{U}(2p)$, where \tilde{U} is the Fourier transform of the effective potential $U(x)$. To have a better understanding of this scattering phenomenon, we proceed to carry out a higher-order Born approximation in the following section.

2. Higher-order Born approximation

For the higher-order Born approximation, we found the momentum representation useful for the states. The starting point is the equation for the outscattering states Eq. (35), where the term $\langle \mathbf{p} | \hat{T} | \Phi_{\text{in}} \rangle$ is determined approximately by using the series approximation of the recursive equation for the transition operator Eq. (32), that is,

$$\begin{aligned} \langle \mathbf{p} | \hat{T} | \Phi_{\text{in}} \rangle &= \langle \mathbf{p} | \hat{V} | \Phi_{\text{in}} \rangle + \langle \mathbf{p} | \hat{V} \hat{G} \hat{V} | \Phi_{\text{in}} \rangle + \dots \\ &+ \langle \mathbf{p} | \hat{V} \hat{G} \hat{V} \dots \hat{V} \hat{G} \hat{V} | \Phi_{\text{in}} \rangle + \dots, \end{aligned} \quad (40)$$

where we have defined the resolvent operator $\hat{G} := 1/(E - \hat{H}_0 + i\epsilon)$. Now, for each term of \hat{G} of the last expansion, one introduces two completeness relations in momentum space $\mathbb{1} = \sum_{\mathbf{q}} |\mathbf{q}\rangle \langle \mathbf{q}|$, where $\sum_{\mathbf{q}} = \frac{1}{2\pi} \sum_m \int \frac{dq}{2\pi}$ and $|\mathbf{q}\rangle := |q, m\rangle$. These completeness relations are introduced before and after the operator \hat{G} . Thus, one has the first term $\tau_1(p) := \langle \mathbf{p} | \hat{V} | \Phi_{\text{in}} \rangle$ and the $(n + 1)$ th term, with $n \geq 1$, has the following structure:

$$\begin{aligned} \tau_{n+1}(p) &:= \sum_{\mathbf{q}^{(1)}, \dots, \mathbf{q}^{(2n)}} \langle \mathbf{p} | \hat{V} | \mathbf{q}^{(1)} \rangle \langle \mathbf{q}^{(1)} | \hat{G} | \mathbf{q}^{(2)} \rangle \\ &\times \langle \mathbf{q}^{(2)} | \hat{V} \dots \hat{V} | \mathbf{q}^{(2n-1)} \rangle \langle \mathbf{q}^{(2n-1)} | \hat{G} | \mathbf{q}^{(2n)} \rangle \\ &\times \langle \mathbf{q}^{(2n)} | \hat{V} | \Phi_{\text{in}} \rangle. \end{aligned} \quad (41)$$

Now, one can reduce half of the integrals since for each term $\langle \mathbf{q}^{(i)} | \hat{G} | \mathbf{q}^{(j)} \rangle = \mathbb{G}(q^i) \delta_{\mathbf{q}^i, \mathbf{q}^j}$, where $\mathbb{G}(q^j) = 1/(E - H_0(\mathbf{q}) + i\epsilon)$. Thus, $(n + 1)$ - th can be simplified as follows:

$$\begin{aligned} \tau_{n+1}(p) &= \sum_{\mathbf{q}^{(1)}, \dots, \mathbf{q}^{(n)}} \langle \mathbf{p} | \hat{V} | \mathbf{q}^{(1)} \rangle \left(\prod_{\ell=1}^{n-1} \mathbb{G}(q^\ell) \langle \mathbf{q}^{(\ell)} | \hat{V} | \mathbf{q}^{(\ell+1)} \rangle \right) \\ &\times \mathbb{G}(q^{(n)}) \langle \mathbf{q}^{(n)} | \hat{V} | \Phi_{\text{in}} \rangle, \end{aligned} \quad (42)$$

where the state $|\mathbf{q}^\ell\rangle = |q^\ell, m^\ell\rangle$ for $\ell = 1, 2, \dots, n$. To simplify the last expression, it is necessary to find the following two generic expressions: (a) $\langle \mathbf{p} | \hat{V} | \mathbf{q} \rangle$ and (b) $\langle \mathbf{p} | \hat{V} | \Phi_{\text{in}} \rangle$. The momentum states are expressed by $|\mathbf{p}\rangle = |p, m\rangle$ and, similarly, $|\mathbf{q}\rangle = |q, m'\rangle$. Thus, for the terms, type (a) can be written as $\langle \mathbf{p} | \hat{V} | \mathbf{q} \rangle = (2\pi) \hbar v_F \sigma_2 m_\tau \delta_{mm'} \langle p | \hat{U}(x) | q \rangle$, where we have acted the total angular momentum operator $\hat{J}_{\theta, \tau} |m\rangle = \hbar m_\tau |m\rangle$ and introduced the orthogonal relation $\langle m | m' \rangle = 2\pi \delta_{mm'}$. Now, we introduce the completeness relation $\mathbb{1} = \int dx |x\rangle \langle x|$ and we use $\langle x | p \rangle = e^{ipx}$, thus one has

$$\langle \mathbf{p} | \hat{V} | \mathbf{q} \rangle = (2\pi) \hbar v_F \sigma_2 m_\tau \delta_{mm'} \tilde{U}(p - q); \quad (43)$$

$\tilde{U}(q) := \int dx e^{-iqx} U(x)$ being the Fourier transform of the potential. Now, for the type-(b) terms, one introduces a completeness relation in the momentum space such that $\langle \mathbf{p} | \hat{V} | \Phi_{\text{in}} \rangle = \sum_{\mathbf{q}} \langle \mathbf{p} | \hat{V} | \mathbf{q} \rangle \langle \mathbf{q} | \Phi_{\text{in}} \rangle$. Now, it is necessary to calculate the term $\Psi_{\text{in}}(\mathbf{q}) = \langle \mathbf{q} | \Phi_{\text{in}} \rangle$, which is the

Fourier transform of the initial wave $e^{i\sigma|k|x} f_m v_{\mu,\sigma}$, that is, $\Psi_{\text{in}}(\mathbf{q}) = 2\pi\delta(q - \sigma|k|) f_m v_{\mu,\sigma}$, thus one has

$$\langle \mathbf{p} | \hat{V} | \Phi_{\text{in}} \rangle = \hbar v_F \sigma_2 v_{\mu,\sigma} f_m m_\tau \tilde{U}(p - \sigma|k|). \quad (44)$$

Notice that the right-hand side of the last equation corresponds to the first term in the series Eq. (40), that is,

$$\tau_1(p) = \hbar v_F f_m (i\mu m_\tau) \tilde{U}(p + |k|) v_\mu, \quad (45)$$

where we have put $\sigma = -1$ since we have an initial left wave, and where we have used the identity $\sigma_2 v_{-\mu} = i\mu v_\mu$. Now, we introduce the terms types (a) Eq. (43) and (b) Eq. (44) in the $(n+1)$ th term $\tau_{n+1}(p)$ (42). Now, again one has to put $\sigma = -1$, and following the straightforward calculation developed in Appendix B, one is able to find

$$\tau_{n+1} = \hbar v_F f_m (i\mu m_\tau)^n m_\tau \tilde{U}(p - |k|) \tilde{U}(2|k|) |\tilde{U}(2|k|)|^{n-1} v_{-\mu} \quad (46)$$

for odd n , whereas

$$\tau_{n+1} = \hbar v_F f_m (i\mu m_\tau)^{n+1} \tilde{U}(p + |k|) |\tilde{U}(2|k|)|^n v_\mu \quad (47)$$

for even n , where $|\cdot|$ is the complex norm. In this manner, the series (40) is $\langle \mathbf{p} | \hat{T} | \Phi_{\text{in}} \rangle = \sum_{n=0}^{\infty} \tau_{n+1}(p)$. This expectation value must be introduced in the LS Eq. (35). Afterward, one needs to compute the Fourier transform to find an expression of the Dirac wave

$$\Phi_m^{\tau(\mu)}(x) = e^{-i|k|x} f_m v_{-\mu} + \sum_{n=0}^{\infty} C_{n+1}(x), \quad (48)$$

where one has still to compute the inverse Fourier transform $C_{n+1}(x) = \int \frac{dp}{2\pi} e^{ipx} \mathbb{G}(p) \tau_{n+1}(p)$. See Appendix B for detailed integral calculations. Thus, the result for $C_{n+1}(x)$ is the following, for odd integers $n = 2j + 1$:

$$C_{2j+2}(x) = (-1)^{j+1} (m_\tau^2 |\tilde{U}(2|k|)|^2)^{j+1} f_m e^{-i|k|x} v_{-\mu}, \quad (49)$$

while for even integers $n = 2j$,

$$C_{2j+1}(x) = (-1)^{j+1} m_\tau \tilde{U}(2|k|) (m_\tau^2 |\tilde{U}(2|k|)|^2)^j f_m e^{i|k|x} v_\mu \quad (50)$$

for $j \in \mathbb{N} \cup \{0\}$. Now, after inserting these expressions in Eq. (48), it is noticeable that each of the factors appearing in front of the ongoing ($e^{-i|k|x}$) and incoming ($e^{i|k|x}$) terms can be cast as a geometric series that can be summed up as $\sum_{\ell=0}^{\infty} (-1)^\ell a^\ell (m_\tau, k) = 1/(1 + a(m_\tau, k))$ while $a(m_\tau, k) < 1$, where $a(m_\tau, k) = m_\tau^2 |\tilde{U}(2|k|)|^2$. Thus, the final expression for the Dirac wave is

$$\Phi_m^{\tau(\mu)}(x) = f_m [\mathcal{F}(m_\tau, k) e^{-i|k|x} v_{-\mu} + \mathcal{G}(m_\tau, k) e^{i|k|x} v_\mu], \quad (51)$$

where the coefficients $\mathcal{F}(m_\tau, k)$ and $\mathcal{G}(m_\tau, k)$ are given by

$$\mathcal{F}(m_\tau, k) = \frac{1}{1 + m_\tau^2 |\tilde{U}(2|k|)|^2}, \quad (52)$$

$$\mathcal{G}(m_\tau, k) = m_\tau \tilde{U}(2|k|) \mathcal{F}(m_\tau, k). \quad (53)$$

The Born approximation Eq. (39) is recovered when $\mathcal{F}(m_\tau, k) \approx 1$. This is expected to be achieved for large values of momenta $|k|$.

Since one can prepare an initial Dirac wave with values of m and k such that $a(m, k) \geq 1$, here we consider an analytical continuation of the geometric series to take into account values of m and k under the last condition. This analytical continuation means that the factors $\mathcal{F}(m, k)$ and $\mathcal{G}(m, k)$ have the same function for values of (m, k) in a region where $a(m, k) \geq 1$.

VI. TRANSMISSION OF THE DIRAC WAVES THROUGH THE GEOMETRY OF A BOUR SURFACE

In this section, using the LS formalism developed above, we carry out a transmission analysis of the Dirac waves on the geometry of Bour surfaces, considering the propagation, taking into account each valley.

A. Nöether current J^μ on the curved nanostructured material

We introduce the Nöether current J^μ of the Dirac Eq. (10) as the probability current density. This quantity is introduced to study how the initial Dirac wave is propagated along the surface. In particular, we can determine the transmission and reflection coefficients using the current J^μ . This conserved quantity is given by [57]

$$J^\mu = \bar{\chi} \Gamma^\mu \chi, \quad (54)$$

even in the presence of a gauge field \mathbb{A}_μ , where $\bar{\chi} = \chi^\dagger \Gamma^0$. Considering both Dirac fields, the Nöether current is given by [57]

$$J^\mu = \sum_{\tau=\pm} \bar{\Psi}^\tau \underline{\gamma}^\mu \Psi^\tau, \quad (55)$$

where $\bar{\Psi}^\tau = \Psi^{\tau\dagger} \underline{\gamma}^0$. Also, we recall that $\underline{\gamma}^\mu$ are given in terms of the vielbeins and the Dirac matrices γ^A introduced above in Sec. III A. Also, recall that $\Psi^\tau(x) = r^{-1/2} \Lambda^{-1/2} \Phi^\tau$, where Λ is the conformal factor introduced above. The zero component of the current, $J^0(x)$, allows us to determine the probability density function, whereas the spatial components of the current allow us to determine how the Dirac wave propagates through the space geometry, that is, using the spatial components one can define the reflection coefficient as

$$\mathcal{R} = \left| \frac{J_{\text{ref}}^a n_a}{J_{\text{inc}}^b n_b} \right| \quad (56)$$

and the transmission coefficient by its complement $\mathcal{T} = 1 - \mathcal{R}$, where \mathbf{n} is a tangent vector on the surface that is normal to a curve γ embedded on the surface. In particular, for the Bour surface, we choose γ to be an r -constant curve; thus \mathbf{n} is a tangent vector along the θ direction. See Fig. 4 to see level curves with the r constant and θ constant on the catenoid, B_1 , and Enneper surfaces.

In the following, we focus on determining the general expressions for the probability density J^0 , transmission coefficient \mathcal{T} , reflection coefficient \mathcal{R} , and conductance G for the Bour surfaces, where particular emphasis is made on the catenoid/helicoid, B_1 -Bour, and classical Enneper surface.

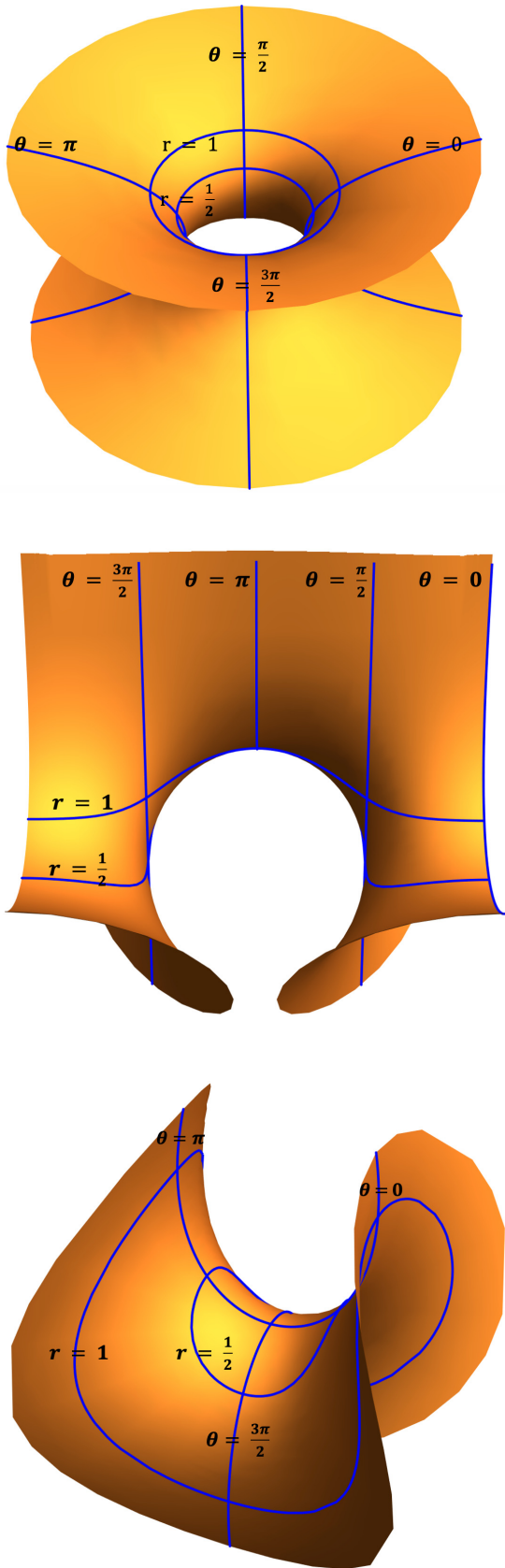


FIG. 4. Catenoid, B_1 -Bour, and classical Enneper minimal surface, from the top to the bottom, drawn with the parametrizations (D1), (D4), and (D3). Each of the surfaces includes examples of level curves with r and θ constant.

B. Probability density function J^0

Before presenting the result for the probability density function, let us obtain normalization factors \mathcal{N}_0 , for the free wave Eq. (29), and \mathcal{N} for the scattered wave Eq. (51). For this purpose, consider a large portion of the area of the surface, and let us impose the condition $\int_{\mathcal{D}} dAJ^0 = 1$, where $dA = r\Lambda(r)drd\theta$ is the area element in the surface. This condition guarantees that a Dirac fermion is surely, at some point, $(r, \theta) \in \mathcal{D} = [0, L] \times [0, 2\pi]$, from the domain \mathcal{D} .

Now, the zero component of the Nöether current is the probability density function given for our particular space-time geometry [see Eq. (12)] by $J^0(r) = \frac{1}{v_F} \sum_{\tau=\pm} \Psi_m^{\tau\dagger(\mu)} \Psi_m^{\tau(\mu)}$. Thus, for the free initial wave one has the density $J^0(r) = \frac{2\mathcal{N}_0^2 |f_m|^2}{v_F r \Lambda}$, thus the normalization factor is easily obtained as $\mathcal{N}_0 = (v_F / (2\pi L))^{\frac{1}{2}} / \sqrt{2} |f_m|$, while for the scattered wave $J^0(r) = \frac{\mathcal{N}^2 |f_m|^2}{v_F r \Lambda} \sum_{\tau=\pm} \mathcal{F}(m_\tau, k)$ the normalization factor is given by $\mathcal{N} = \mathcal{N}_0 / \sqrt{\sum_{\tau=\pm} \mathcal{F}(m_\tau, k)}$. Now, the probability density function is given for both waves the probability density by the expression

$$J^0(r, \theta) = \frac{1}{2\pi L r \Lambda(r)}, \quad (57)$$

which means that it is most probable to find Dirac particles near the scattering center on the Bour surface. It is noteworthy to mention that the scattering point ($x \simeq 0$) corresponds to the point where the curvature attains its maximum value [see Fig. 1)].

C. Transmittance and conductance on the Bour geometries

Now we want to determine the reflection and the transmission coefficients. We choose γ as the r -constant curve on a Bour surface; thus, the normal vector to γ is tangent to a θ -constant curve. Notice that $J^\theta = -\frac{1}{r^2 \Lambda^2} \sum_{\tau=\pm} \Phi_m^{\tau\dagger(\mu)} \sigma_1 \Phi_m^{\tau(\mu)}$ after using $\underline{\gamma}^\theta = \gamma^2 e_1^\theta$, where the vielbein in this case is $e_1^\theta = 1/\Lambda$. Now, recalling that $\sigma_1 v_\mu = \mu v_\mu$ and $v_\mu^\dagger v_\mu = 1$, we compute the incidence current J_{inc}^θ using the initial wave $\mathcal{N}_0 e^{-i|k|x} f_m v_{-\mu}$,

$$J_{\text{inc}}^\theta = \frac{v_F \mu}{(2\pi L) r^2 \Lambda^2}, \quad (58)$$

and compute J_{ref}^θ using the reflection wave $\mathcal{N} f_m \mathcal{G}(m, k) e^{i|k|x} v_\mu$, getting

$$J_{\text{ref}}^\theta = -\frac{v_F \mu}{(2\pi L) r^2 \Lambda^2} \frac{\sum_{\tau=\pm} |\mathcal{G}(m_\tau, k)|^2}{\sum_{\tau=\pm} \mathcal{F}(m_\tau, k)},$$

where recall that $m_\tau = m + \frac{\tau\varphi}{2\pi}$, φ being the non-Abelian flux, and $\mathcal{G}(m_\tau, k)$ and $\mathcal{F}(m_\tau, k)$ are given by Eqs. (53) and (52). Now, using the reflection coefficient definition Eq. (56), it is not difficult to get

$$\mathcal{R} = \frac{|\mathcal{G}(m_+, k)|^2 + |\mathcal{G}(m_-, k)|^2}{\mathcal{F}(m_+, k) + \mathcal{F}(m_-, k)}. \quad (59)$$

Both coefficients \mathcal{R} and \mathcal{T} can be expressed in terms of the Fourier transform $\tilde{U}(p) = \int_{-\infty}^{\infty} dx e^{-ipx} U(x)$, thus it is convenient to make further simplifications. Since the potential is proportional to $1/|c|$, it is convenient to perform the following

change of variable $\tilde{x} = x/|c|$, thus let us define the function

$$\mathcal{U}(\xi) = \int_{-\infty}^{\infty} d\tilde{x} e^{-i\xi\tilde{x}} |c| U(|c|\tilde{x}). \quad (60)$$

Now, instead of using the wave number k , we use the energy dispersion relation $E = \pm \hbar v_F |k|$. Also, notice that the Bour material introduces a natural scale of energy given by $E_0 = \hbar v_F / |c|$ in terms of the characteristic length, $|c|$, associated to each Bour surface. Therefore, the reflection and transmission coefficients in terms of the energy E are given for any Bour surface within the present approximation as

$$\mathcal{R}(E) = 1 - \mathcal{T}(E), \quad (61)$$

$$\mathcal{T}(E) = \frac{\frac{1+m_-^2}{1+m_+^2} |\tilde{U}(2E_*)|^2}{2 + (m_-^2 + m_+^2) |\tilde{U}(2E_*)|^2} + \frac{\frac{1+m_+^2}{1+m_-^2} |\tilde{U}(2E_*)|^2}{2 + (m_-^2 + m_+^2) |\tilde{U}(2E_*)|^2}. \quad (62)$$

where $E_* = |E|/E_0$ is a dimensionless parameter. The conductance can be computed using the simple expression $G(E) = \frac{e^2}{\pi \hbar} \mathcal{T}(E)$. Notice that each Bour material with typical characteristic length $|c|$ introduces a natural scale of energy $E_0 = \hbar v_F / |c|$; for surfaces with $|c| \sim 1$ nm the characteristic scale energy is $E_0 \sim 8.27$ eV. Note that for big values of energy, that is, $|E| \gg E_0$, the above result Eqs. (61) and (62) reduces to the Born approximation since in this parameter region one has $\mathcal{R}(E) \simeq \frac{m_+^2 + m_-^2}{2} |\mathcal{U}(2E_*)|^2$ and $\mathcal{T}(E) \simeq 1 - \frac{m_+^2 + m_-^2}{2} |\mathcal{U}(2E_*)|^2$, which is the Born approximation result. In addition, in the case $|m| \gg \varphi/2\pi$ ($|m| \ll \varphi/2\pi$), the reflection and transmission are given by

$$\mathcal{R}(E) \simeq \frac{\underline{m}^2 |\mathcal{U}(2E_*)|^2}{1 + \underline{m}^2 |\mathcal{U}(2E_*)|^2}, \quad (63)$$

$$\mathcal{T}(E) \simeq \frac{1}{1 + \underline{m}^2 |\mathcal{U}(2E_*)|^2}, \quad (64)$$

where $\underline{m} = \max(|m|, \frac{\varphi}{2\pi})$. In the case $\underline{m} = |m|$, the topological defects do not affect the reflection and transmission behavior. In the opposite case, $\underline{m} = \varphi/2\pi$, topological defects dominate the reflection and transmission coefficients; in particular, they scatter out the Dirac particles such that for a large N number of defects $\mathcal{T} \propto N^{-2}$ and $\mathcal{R} \propto 1 + O(N^{-1})$, while energy E_* such that $\mathcal{U}(2E_*) \neq 0$.

Now, we still need to compute the Fourier transform of the effective potential. Conspicuously, for any Bour surface, it is useful to go back to the original radial coordinate instead of x since $dx = \Lambda(r) dr$ and the effective potential $V(r) = 1/(r\Lambda(r))$, thus the Fourier transform is

$$\mathcal{U}(\xi) = \int_0^\infty \frac{dr}{r} \exp\left[-i\xi \frac{x_n(r)}{|c|}\right], \quad (65)$$

where for each Bour surface labeled with n , $x_n(r)$ is the change of variable introduced above [see, for instance, Eq. (18) for $n \neq 1$].

1. Transmission on the catenoid/helicoid

In this case, one has $x_0(r) = |c|(r - r^{-1})$. Here, it is convenient to make the change of variable $y = \log r \in \mathbb{R}$, thus the argument of the exponential in Eq. (65) turns out to be the odd function $\sinh(y)$, meaning that the Fourier transform

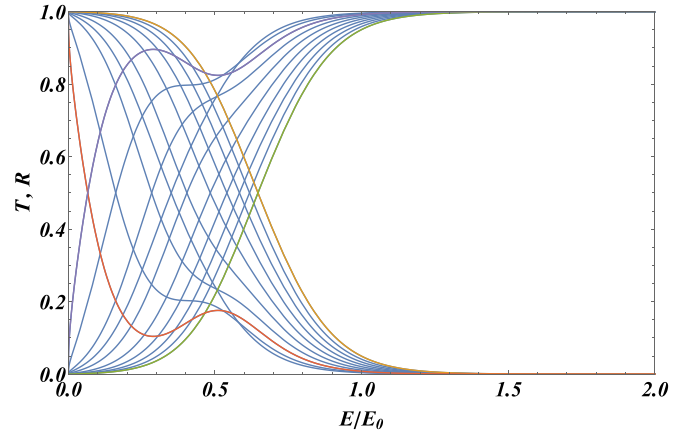


FIG. 5. Family of transmission and reflection coefficients [Eqs. (61) and (62)] versus reduced energy $E_* = E/E_0$ using the Fourier transform Eq. (66) corresponding to the catenoidal/helicoidal geometry. The set of curves was obtained for cases with $m = 1, \dots, 10$, and for the effective gauge flux $\frac{\varphi}{2\pi} = \frac{8}{3}$. The orange and green curves are guides for the eyes to identify the $m = 10$ case.

is simplified to $\mathcal{U}(\xi) = \int_{-\infty}^{\infty} dy \cos[2\xi \sinh(y)]$. This integral can be expressed in terms of a modified Bessel function [68]:

$$\mathcal{U}(\xi) = 2K_0(2\xi). \quad (66)$$

Figure 5 shows the reflection and transmission coefficient for a propagation wave through the catenoid, where we have used Eq. (66). In addition, one can see that the value of $E_* = E_x$, where the transmission and reflection have the same value, is translated to the right as long as the value of m increases. The interception value of energy is E_x , where the transcendental equation is satisfied, $\mathcal{T}(E_x) = \frac{1}{2}$, as can appreciate in Fig. 5.

2. Transmission on B_1 -Bour

In this case, one has $x_1(r) = |c|(\log r + \frac{1}{2}r^2)$. Let us substitute $i\xi \rightarrow z$, where z is a complex value with $\text{Re} z < 0$. Additionally, it is convenient to make the change of variable $y = r^2 \in \mathbb{R}^+$, thus the integral Eq. (65) turns out to be $\mathcal{U}(\xi) = 2 \int_0^\infty \frac{dy}{y} y^{-\frac{z}{2}} e^{-\frac{z}{2}y}$, which can be related to a gamma function [68] as

$$\mathcal{U}(\xi) = \lim_{z \rightarrow i\xi} 2 \left(\frac{z}{2}\right)^{\frac{z}{2}} \Gamma\left(-\frac{z}{2}\right). \quad (67)$$

Since we need the complex norm of $\mathcal{U}(\xi)$, we use the identity $|\Gamma(iy)|^2 = \pi/(y \sinh(\pi y))$ for $y \in \mathbb{R}$ [68], and it remains to compute the complex norm of the factor in Eq. (67); by straightforward elementary calculation one has $(\frac{z}{2})^{\frac{z}{2}} = e^{i\frac{\xi}{2} \log \frac{\xi}{2}} e^{-\frac{\xi\pi}{4}}$. Therefore,

$$|\mathcal{U}(\xi)|^2 = \frac{4}{\xi(e^{\pi\xi} - 1)}. \quad (68)$$

Figure 6 shows the reflection and transmission coefficient for a propagation wave through the B_1 -Bour surface, where we have used Eq. (68). The structure of these curves is very similar to the previous case. The principal difference corresponds to that the total transmission occurs to a bigger value

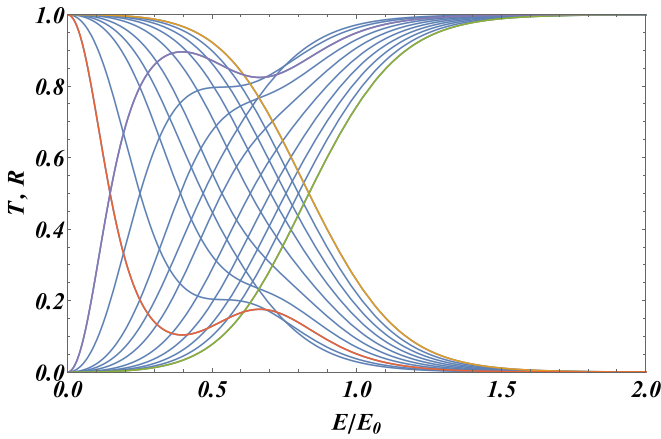


FIG. 6. Family of transmission and reflection coefficients [Eqs. (61) and (62)] versus reduced energy $E_* = E/E_0$ using the Fourier transform Eq. (67) corresponding to the B_1 geometry. The set of curves was obtained for cases with $m = 1, \dots, 10$, and for the non-Abelian flux $\frac{\varphi}{2\pi} = \frac{8}{3}$. The orange and green curves guide the eyes to identify the $m = 10$ case.

of E_* . In addition, how the curves are moving to the left is given according to the transcendental equation $\mathcal{T}(E_K) = 1/2$.

3. Transmission on the classical Enneper surface and $n > 2$ Bour surfaces

In this case, one has $x_n(r) = |c|(\frac{r^{n-1}}{n-1} + \frac{r^{n+1}}{n+1})$ with $n \geq 2$, thus the Fourier transform reduces to the integral

$$U(\xi) = 2 \int_0^\infty \frac{dr}{r} \cos\left(\xi \left(\frac{r^{n-1}}{n-1} + \frac{r^{n+1}}{n+1}\right)\right). \quad (69)$$

This integral is strictly divergent due to the singularity at $r = 0$. The integral is regularized, introducing an inferior cutoff such that $r \geq \epsilon$.

Classical Enneper case. To isolate the singular part, let us consider the next approximation. First, let us focus on the classical Enneper surface $n = 2$. One can argue that the most important contribution to the integral is near $r = \epsilon$, where the cubic term of the cosine argument may be neglected since $r^3 \simeq \epsilon^3$; moreover, for large r value, the contributions to the integral decay to zero as r^{-1} . Using this rationale, let us ignore the cubic term inside the argument of the cosine function; thus, the integral reduces to the cosine integral

$$U(\xi) \simeq 2 \int_\epsilon^\infty \frac{dr}{r} \cos(\xi r) := -2\text{Ci}(\epsilon\xi), \quad (70)$$

where $\text{Ci}(x)$ is the cosine integral that has the series expansion $\text{Ci}(x) = \gamma + \log x + \sum_{n=1}^\infty (-1)^n x^{2n} / (2n(2n!))$ [68]. Thus, one has

$$U(\xi) \simeq -2(\gamma + \log(\xi)) + 2 \log(1/\epsilon) + O(\epsilon^2), \quad (71)$$

where γ is the Euler-Mascheroni constant. Therefore, the singular part is given by $2 \log(1/\epsilon)$. Now, we performed a numerical evaluation of Eq. (69), subtracting the singular part and comparing it with the previous result Eq. (71) [see Fig. 7]. The main error is close to $k \simeq 0$, while for the rest of the values, the error is around 1%.

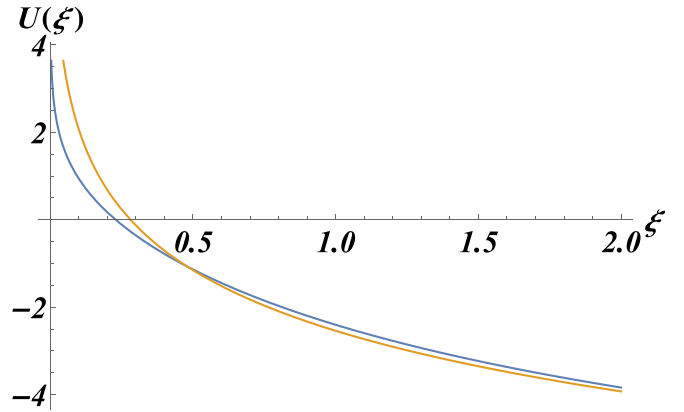


FIG. 7. Fourier transform Eq. (69) versus argument ξ for the classical Enneper geometry with $n = 2$ (blue color curve). It also shows a comparison between the numerical calculation of Eq. (69), and analytical approximation Eq. (71), corresponding to blue and orange curves, respectively.

Figure 8 shows the reflection and transmission coefficient for a propagation wave through the classical Enneper surface, where we have used numerical calculation of the Fourier transform $U(\xi)$. The main feature of the transmission curves for the classical Enneper surface is the transmission value $\mathcal{T}(E_K) = 1$ at energy E_K showing the Klein tunneling phenomena in this case [69]. The Klein value E_K corresponds to the value where the Fourier transform $U(\xi)$ vanishes [see Fig. 7]. Using the approximation Eq. (71), one can estimate the value of $E_K \simeq \frac{E_0}{2} e^{-\gamma} \approx 0.28E_0$, with an error of 5% respect to the numerical calculation. However, in contrast to the previous cases, catenoid and B_1 -Bour surfaces, in the present case, show a strong suppression of the transmission for values above the Klein value E_K , giving rise to a total reflection effect

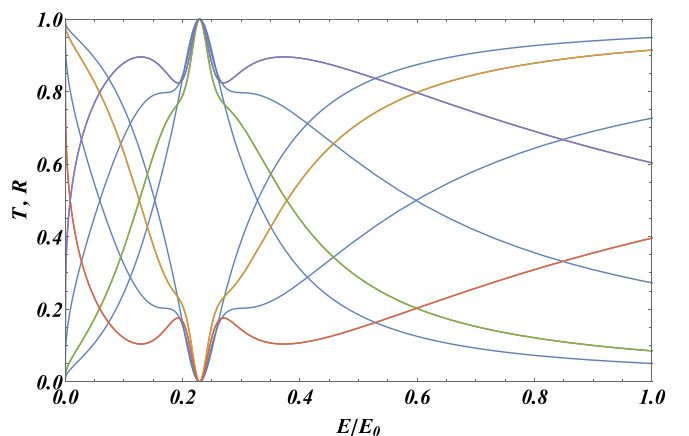


FIG. 8. Family of transmission and reflection coefficients [Eqs. (61) and (62)] versus reduced energy $E_* = E/E_0$ using the numerical evaluation of the Fourier transform Eq. (72) corresponding to the classical Enneper geometry with $n = 2$. The set of curves was obtained for cases with $m = 1, 2, 3, 4$, and for the non-Abelian flux $\frac{\varphi}{2\pi} = \frac{8}{3}$. The purple and green curves guide the eyes to identify the $m = 3$ and $m = 4$ cases, respectively. For all transmission curves, we identify the same single Klein point $E_K \simeq 0.23E_0$, where the transmission is 1 and a clear trend of suppression after such a point.

and thus vanishing conductance $G(E) \rightarrow 0$ for $E \gg E_K$. In addition, one can observe the Fig. 8 oscillations for the modes m near the value of $\varphi/2\pi$, whereas for values of m far from φ the behavior of reflection and transmission follow Eqs. (63) and (64), without changing the conclusion of the existence of the Klein point. Indeed, for $|m| \gg \varphi/2\pi$, there are two interception values, and both values move towards the Klein value as the m value increases. This effect can be explained using the approximation Eq. (71) by making the condition $m^2 |\mathcal{U}(2E_*(m))|^2 = 1$, thus one obtains the values in terms of m by the equation $E_*(m) \simeq E_K e^{\pm \frac{1}{2m}}$, showing the effect just mentioned.

Bn-Bour cases for $n > 2$. In this case, one can follow the same line of argument as in the Enneper case. For instance, let us perform the change of variable $y = \frac{r^{n-1}}{n-1}$, thus Fourier transforms turn out as

$$\mathcal{U}(\xi) = \frac{2}{n-1} \int_{\epsilon}^{\infty} \frac{dy}{y} \cos(\xi(y + \alpha_n y^{\beta_n})), \quad (72)$$

where $\alpha_n = (n-1)^{\beta_n}/(n+1)$ and $\beta_n = \frac{n+1}{n-1}$. Observe $1 < \beta_n \leq 3$, where equality corresponds to the classical Enneper case. Since $\beta_n > 1$, one can attempt to argue that this term is not dominant near the singularity; thus, in this approximation, one has $\mathcal{U}(\xi) \simeq -2\text{Ci}(\epsilon\xi/(n-1))/(n-1)$, thus the difference between the present case and the Enneper case is a factor of $1/(n-1)$. However, in this case, the error increases more than 10%. Thus, we numerically compute the Fourier transform Eq. (69) in this case.

Figure 9 shows the reflection and transmission coefficient for a propagation wave through the B_3 -Bour and B_4 -Bour surfaces. Like in the classical Enneper case, it can be appreciated that for each B_n -Bour surface, there is a single Klein point $E_{K,n}$, where the transmittance is one. The Klein point moves to the right for greater values of n . After the Klein point $E_{K,n}$, the transmission decreases slowly as n increases; however, it is also wholly suppressed for large energy values.

According to Figs. 8 and 9 and Eq. (62), Klein tunneling is achieved for all m cases, including $m = 1$, which we have associated with quasibound states in the above discussion in Sec. IV. Thus, our explanation for the Klein tunneling on the B_n -Bour surfaces with $n \geq 2$ has to do with the fact that the scattered wave is decomposed into a combination of orthogonal components of the pseudospins $v_{-\mu}$ and v_{μ} [see Eq. (51)] for the reflected and transmitted waves in each valley, respectively, and the fact that $V(x)$ behaves as a Coulomb-type potential which is entirely a consequence of the geometry.

VII. CONCLUDING REMARKS

In this paper, we study the electronic degrees of freedom on a curved sheet of graphene based on the Dirac equation. On this occasion, we propose the hypothetical existence of a graphene sheet with the geometry of a Bour surface; examples of these surfaces are the catenoid, the helicoid, and the classical Enneper surface, among other B_n -Bour surfaces that can be labeled using the n parameter. Bour surfaces belong to the large family of minimal surfaces that minimize the area or solutions of the Willmore shape equation. It is conspicuous that the geometry of the minimal surfaces was proposed to model specific carbon structures in Ref. [14].

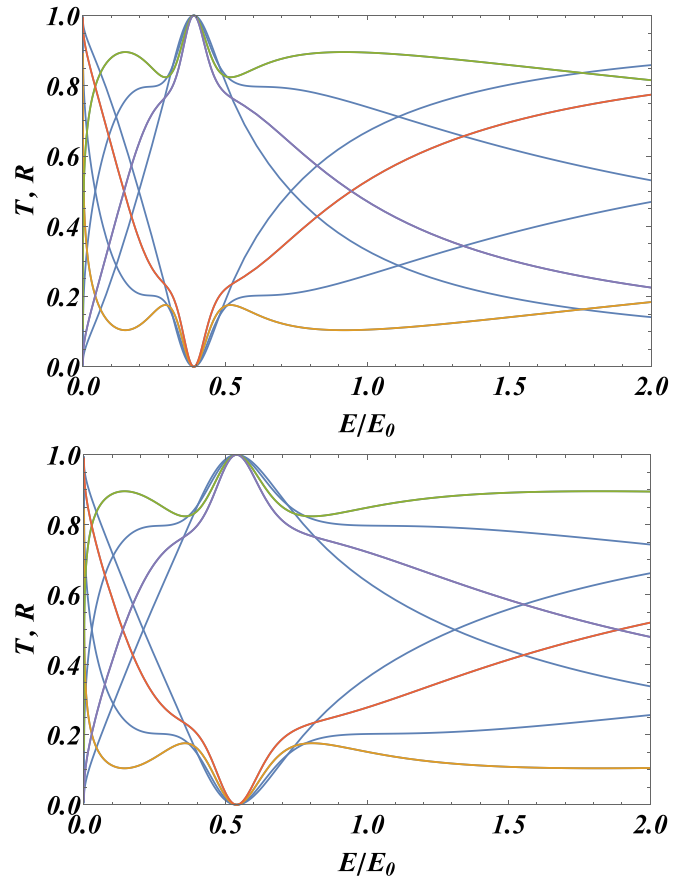


FIG. 9. Family of transmission and reflection coefficients [Eqs. (61) and (62)] versus reduced energy $E_* = E/E_0$ using the numerical evaluation of the Fourier transform Eq. (72) corresponding to the B_3 -Bour surface with $n = 3$ (top) and B_4 -Bour surface with $n = 4$ (bottom). The set of curves was obtained for cases with $m = 1, 2, 3, 4$ and for the non-Abelian flux $\frac{\varphi}{2\pi} = \frac{8}{3}$. The green and purple curves guide the eyes to identify the $m = 3$ and $m = 4$ cases, respectively. For all sets of transmission curves, we identify the same single Klein point $E_K \simeq 0.39E_0$ (top) and $E_K \simeq 0.54E_0$ (bottom), where the transmission is 1, and a clear downward trend in transmission after that point. Moreover, the higher the value of n , the slower the downward trend.

Although there is still no artificial or natural realization of these carbon allotropes in either laboratory or nature, there are good expectations of their existence from numerical and experimental investigations [12,15–17].

Now, for each n , the space-time \mathbb{M} is built with the global structure of $\mathbb{M} = \mathbb{R} \times B_n$ over which we define the Dirac field. In particular, using an elementary change of parameters, it is possible to rewrite the metric of \mathbb{M} as $ds^2 = -v_F^2 dt^2 + dx^2 + (1/V^2(x))d\theta^2$, and the Dirac equation reads

$$i\hbar\partial_t\Phi^\tau = v_F\sigma_1\hat{p}_x\Phi^\tau + v_F V(x)\sigma_2\hat{J}_{\theta,\tau}\Phi^\tau, \quad (73)$$

where v_F is the Fermi velocity and σ_1 and σ_2 are the Pauli matrices. In this equation, $V(x)$ has been interpreted as an effective scattering potential coupled to a pseudospin orbit term of the form $\sigma_2\hat{J}_{\theta,\tau}$, where σ_2 the direction of the pseudospin and $\hat{J}_{\theta,\tau} = \hat{\ell}_\theta + \tau\frac{\varphi}{2\pi}\hat{h}$ is a total angular momentum in two dimensions, φ being the non-Abelian gauge flux due to the

topological defects, and τ the valley index. For each Bour surface, it was found that $V(x)$ decays to zero as $x \rightarrow \infty$, while $V(x)$ works as a potential barrier near $x = 0$. It can be shown that for $n \geq 2$, $V(x)$ approach a repulsive Coulombic-type potential.

The asymptotic behavior of the states in $x \rightarrow \infty$ is determined with Eq. (73), which effectively corresponds to solutions of a Dirac equation in a space-time 1 + 1. These states in terms of x are characterized as plane waves with a pseudospin up \uparrow (or down \downarrow) depending on the positive or negative value of the energy. Furthermore, through the LS formalism, we studied the outscattering states, giving rise to an outscattering state divided into a transmitted and a reflected wave. This is done through the Born and the high-order Born approximation, which can be summed up. In particular, it is observed that the reflected wave transmutes the pseudospin direction, which we coined the spin-orbit interaction.

In addition, through the Nöether current J^μ , the probability density, J^0 , is determined, which allows us to argue that it is more probable to find Dirac fermions near the scattering point, in fact, within this approximation we found that the probability density is proportional to $V(x)$. Now, using the spatial components of J^μ , the incident and scattered currents are determined to find expressions for the reflectance $\mathcal{R}(E)$ and the transmittance $\mathcal{T}(E)$, respectively. As expected [70], $\mathcal{R}(E)$ and $\mathcal{T}(E)$ depend on the number of topological defects, N . It is found that for the Bour surfaces B_0 , catenoid (or helicoid), and B_1 -Bour, there is usual behavior for the transmittance and reflectance, giving rise to the effect of total transmittance for large values of energy. Although the potential barrier in the cases B_0 and B_1 evokes the usual situation where Klein's tunneling arises, the difference lies in the coupling with σ_2 that appears in Eq. (73), which we coin the absence of Klein's tunneling [69]. However, for Bour surfaces B_n with $n \geq 2$, including the classical Enneper surface, we show that there is an energy point E_K for which the transmittance is equal to $\mathcal{T}(E_K) = 1$, giving rise to a manifestation of Klein's tunneling. In contrast, for large values of energy $E \gg E_K$, the transmittance decays to zero, suppressing the conductance completely. Furthermore, it is found that the transmittance $\mathcal{T}(E) \propto N^{-2}$ for large numbers of topological defects on all

surfaces B_n , as long as the energy is different than the Klein point, $E \neq E_K$.

The present paper can be extended as follows. For $n \geq 2$, one can approximate the geometry-induced potential $V(x)$ as a Coulombic potential near the scattering region, where one can attempt to figure out an analytical solution for the states and the electronic spectrum. Following a different direction, through the WE representation, we can propose the study of electronic degrees of freedom on other minimal surfaces, such as simply periodic minimal surfaces, k-noids, or Schwartzites that are much more involved. In particular, for these surfaces, it is found that the conformal factor $\Lambda(r, \theta)$ depends intricately on r and θ , so it is not possible to perform a separation as in the case of Bour surfaces [56]. However, we can implement traditional methods like the finite element to solve the Dirac Eq. (17) to study other electronic properties like the density of states, Kubo conductivity, etc.

ACKNOWLEDGMENTS

The authors acknowledge both reviewers for their valuable comments and suggestions. V.A.G-D. acknowledges the financial support provided by Conahcyt (No. CVU 736886). P.C.-V. would like to thank I. Huet-Hernández and R. de Coss for many valuable discussions. P.C.-V. the financial support provided by SNI-Conahcyt (No. 92896).

APPENDIX A: GREEN'S FUNCTION CALCULATION

Calculation of the one-dimensional Green's function. Let us start with the equation $(E - v_F \sigma_1 \hat{p}_x) \mathbb{G}(x, x', E) = \delta(x - x')$, where the momentum operator $\hat{p}_x = -i\hbar \partial_x$, and let us recall that the dispersion relation is given by $E = \pm \hbar v_F |k|$. Now, let us define the function $g_0(x, x', E)$ such that $\mathbb{G}(x, x', E) = (E + v_F \sigma_1 \hat{p}_x) g_0(x, x', E)$, thus it is not difficult to show that $g_0(x, x', E)$ satisfies the Green's-Helmholtz equation $(\hbar v_F)^2 (-\partial_x^2 + k^2) g_0(x, x', E) = \delta(x - x')$. Now, the solution of this equation is known to be [71]

$$g_0(x, x', E) = \frac{1}{2i(\hbar v_F)^2 |k|} e^{i|k||x-x'|}. \quad (\text{A1})$$

APPENDIX B: CALCULATION OF THE HIGHER-ORDER BORN APPROXIMATION

1. Calculation of $\tau_{n+1}(p)$ terms

We start with the expression Eq. (42),

$$\begin{aligned} \tau_{n+1}(p) &= (\hbar v_F)^{n+1} (2\pi)^n \sum_{\mathbf{q}^{(1)}, \dots, \mathbf{q}^{(n)}} \sigma_2 m_\tau \delta_{m m^{(1)}} \tilde{U}(p - q^{(1)}) \left(\prod_{\ell=1}^{n-1} \mathbb{G}(q^{(\ell)}) \sigma_2 m_\tau^\ell \delta_{m^{(\ell)} m^{(\ell+1)}} \tilde{U}(q^{(\ell)} - q^{(\ell+1)}) \right) \\ &\quad \times \sigma_2 v_{\mu\sigma} f_m^{(n)} m_\tau^{(n)} \tilde{U}(q^{(n)} - \sigma |k|), \end{aligned} \quad (\text{B1})$$

where we have substituted the expression for type (a) Eq. (43) and type (b) Eq. (44). Taking advantage of the Kronecker deltas $\delta_{m^{(\ell)} m^{(\ell+1)}}$, we can simplify the last expression as follows (note that each 2π cancels out with each 2π that appears in $\frac{1}{2\pi} \sum_m$):

$$\begin{aligned} \tau_{n+1}(p) &= (\hbar v_F m_\tau)^{n+1} f_m \int \left(\prod_{\ell=1}^n \frac{dq^{(\ell)}}{2\pi} \right) \sigma_2 \tilde{U}(p - q^{(1)}) \left(\prod_{\ell=1}^{n-1} \mathbb{G}(q^{(\ell)}) \sigma_2 \tilde{U}(q^{(\ell)} - q^{(\ell+1)}) \right) \mathbb{G}(q^{(n)}) \\ &\quad \times \sigma_2 v_{\mu\sigma} \tilde{U}(q^{(n)} - \sigma |k|). \end{aligned} \quad (\text{B2})$$

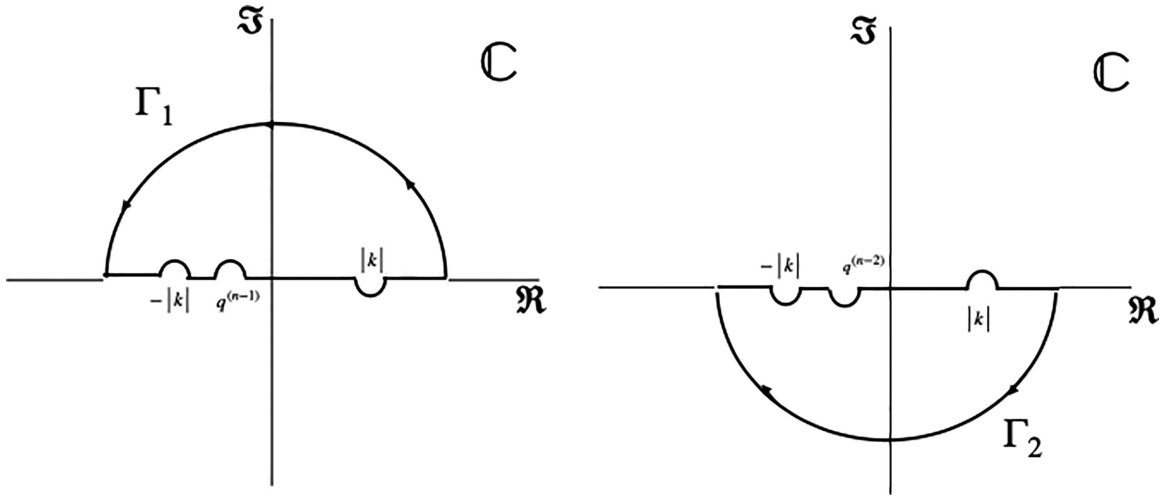


FIG. 10. Contour curves Γ_1 and Γ_2 for the complex integrals in the z plane [Eq. (B4)] and in the q^{n-1} plane [Eq. (B5)], respectively.

Now, we organize the integrals in the following nested structure:

$$\tau_{n+1}(p) = (\hbar v_F m_\tau)^{n+1} f_m \int \frac{dq^{(1)}}{2\pi} \sigma_2 \tilde{U}(p - q^{(1)}) \mathbb{G}(q^{(1)}) \mathcal{U}^{(1)}(q^{(1)}) \sigma_2 v_{\mu\sigma}, \quad (\text{B3})$$

where $\mathcal{U}^{(1)}(q^{(1)})$ is written in terms of $\mathcal{U}^{(2)}(q^{(2)})$, and so on. In general, one has the following definition:

$$\mathcal{U}^{(\ell)}(q^{(\ell)}) = \int \frac{dq^{(\ell+1)}}{2\pi} \sigma_2 \tilde{U}(q^{(\ell)} - q^{(\ell+1)}) \mathbb{G}(q^{(\ell+1)}) \mathcal{U}^{(\ell+1)}(q^{(\ell+1)}),$$

where $\ell = 1, \dots, n-1$ and $\mathcal{U}^{(n)}(q^{(n)}) = \tilde{U}(q^{(n)} - \sigma|k|)$.

Next, let us proceed to calculate $\mathcal{U}^{(n-1)}(q^{(n-1)})$. The integral involved in this quantity can be performed using complex integration, replacing $q^{(n)}$ by the complex variable z ,

$$\mathcal{U}^{(n-1)}(q^{(n-1)}) = i \int_{\Gamma_1} \frac{dz}{2\pi i} \sigma_2 \tilde{U}(q^{(n-1)} - z) \mathbb{G}(z) \tilde{U}(z + |k|), \quad (\text{B4})$$

where we have put $\sigma = -1$ since we have an initial left wave. The contour complex integration Γ_1 is chosen as shown on the left side of Fig. 10, since we exclude the points where the argument of the Fourier transform is zero. Note that $\tilde{U}(0) = \int_{-\infty}^{\infty} dx U(x)$ is strictly divergent since $U(x)$ is a long-range potential which for all Bour surfaces decay as $1/x$. The Green's function $\mathbb{G}(p)$ in momentum space can be written as

$$\mathbb{G}(p) = \frac{\mu}{\hbar v_F} \frac{|k| + \mu \sigma_1 p}{[p - (|k| + i\epsilon)][p + (|k| + i\epsilon)]},$$

where $\mu = \pm$ represents the positive and negative energy states, and one can identify two poles at $|k| + i\epsilon$ and $-|k| - i\epsilon$. Using the Cauchy integral theorem, it is not difficult to show that

$$\mathcal{U}^{(n-1)}(q^{(n-1)}) = \tilde{U}(q^{(n-1)} - |k|) \frac{i\mu}{\hbar v_F} \tilde{U}(2|k|) \sigma_2 \mathbb{P}_\mu,$$

where $\mathbb{P}_\mu = \frac{1}{2}(1 + \mu \sigma_1)$ is a projector. Now, to be transparent in the calculation, let us insert this result into the integration by the q^{n-1} variable, turning it out as

$$\mathcal{U}^{(n-2)}(q^{(n-2)}) = \int \frac{dq^{(n-1)}}{2\pi} \sigma_2 \tilde{U}(q^{(n-2)} - q^{(n-1)}) \mathbb{G}(q^{(n-1)}) \tilde{U}(q^{(n-1)} - |k|) \frac{i\mu}{\hbar v_F} \tilde{U}(2|k|) \sigma_2 \mathbb{P}_\mu.$$

Although the integration is similar to the previous one, it is convenient to perform the change of variable $q^{(n-1)} \rightarrow -q^{(n-1)}$, thus the integration results in

$$\mathcal{U}^{(n-2)}(q^{(n-2)}) = \int \frac{dq^{(n-1)}}{2\pi} \sigma_2 \tilde{U}(q^{(n-2)} + q^{(n-1)}) \mathbb{G}(-q^{(n-1)}) \tilde{U}^*(q^{(n-1)} + |k|) \frac{i\mu}{\hbar v_F} \tilde{U}(2|k|) \sigma_2 \mathbb{P}_\mu, \quad (\text{B5})$$

where $\tilde{U}^*(k) = \tilde{U}(-k)$ is the complex conjugate. Now, we proceed to calculate this integral again using complex integration as in the previous integration. The result is the same except that \mathbb{P}_μ changes by $\mathbb{P}_{-\mu}$, that is,

$$\mathcal{U}^{(n-2)}(q^{(n-2)}) = \tilde{U}(q^{(n-2)} + |k|) \left(\frac{i\mu}{\hbar v_F} \right)^2 |\tilde{U}(2|k|)|^2 \sigma_2 \mathbb{P}_{-\mu} \sigma_2 \mathbb{P}_\mu,$$

where $|\cdot|$ is the complex norm. Now, by an iterative process, one can conclude that

$$\mathcal{U}^{(1)}(q^{(1)}) = \tilde{U}(q^{(1)} + (-1)^{n-1}|k|) \left(\frac{i\mu}{\hbar v_F} \right)^{n-1} \mathbb{B}_\mu^{(n)},$$

where

$$\mathbb{B}_\mu^{(n)} = \begin{cases} \prod_{j=1}^{(n-1)/2} [|\tilde{U}(2|k|)|^2 \sigma_2 \mathbb{P}_{-\mu} \sigma_2 \mathbb{P}_\mu], & \text{for } n \text{ odd} \\ \tilde{U}(2|k|) \sigma_2 \mathbb{P}_\mu \prod_{j=1}^{(n-2)/2} [|\tilde{U}(2|k|)|^2 \sigma_2 \mathbb{P}_{-\mu} \sigma_2 \mathbb{P}_\mu], & \text{for } n \text{ even.} \end{cases} \quad (\text{B6})$$

Note that Eq. (B6) can be simplified further as a consequence of the following algebra: $\sigma_2 \mathbb{P}_\mu = \mathbb{P}_{-\mu} \sigma_2$, thus $\sigma_2 \mathbb{P}_{-\mu} \sigma_2 \mathbb{P}_\mu = \mathbb{P}_\mu \sigma_2^2 \mathbb{P}_\mu = \mathbb{P}_\mu^2 = \mathbb{P}_\mu$. Using this algebra and the property $\mathbb{P}_\mu^2 = \mathbb{P}_\mu$, one obtains

$$\mathbb{B}_\mu^{(n)} = \begin{cases} |\tilde{U}(2|k|)|^{n-1} \mathbb{P}_\mu, & \text{for } n \text{ odd} \\ \tilde{U}(2|k|) |\tilde{U}(2|k|)|^{n-2} \sigma_2 \mathbb{P}_\mu, & \text{for } n \text{ even.} \end{cases}$$

Now, we substitute $\mathcal{U}^{(1)}(q^{(1)})$ inside the expression for $\tau_{n+1}(p)$ in Eq. (B3). We proceed to perform the calculation for n odd and even cases using the same strategy used to calculate the integrals on the variables $q^{(n)}$ and $q^{(n-1)}$. Additionally, we use the property $\mathbb{P}_\mu v_\mu = v_\mu$ and $\sigma_2 v_{-\mu} = i\mu v_\mu$. Thus, the result of the $n+1$ -th term corresponds to the expressions in Eqs. (46) and (47).

2. Calculation of $C_{n+1}(x)$ terms

The starting point to calculate the terms $C_{n+1}(x)$ corresponds to the Fourier integral

$$C_{n+1}(x) = \int \frac{dp}{2\pi} e^{ipx} \mathbb{G}(p) \tau_{n+1}(p)$$

in the cases even n and odd n . For odd n , we use Eq. (46), make the change of variable $p \rightarrow -p$, and perform the complex integration using the contour Γ_2 . In contrast, for even n , we use Eq. (47), and the complex integration is performed using the contour Γ_1 . In this manner, we obtain the desired expressions Eqs. (49) and (50), respectively.

APPENDIX C: ALTERNATIVE SET OF LOCAL COORDINATES

1. Cartesian coordinates

The metric of the space-time \mathbb{M} written through the square of the line element considered here is

$$ds^2 = -v_F^2 dt^2 + \Lambda^2(\omega) |d\omega|^2, \quad (\text{C1})$$

where $\Lambda^2(\omega)$ is the conformal factor introduced above for the minimal surfaces and $|d\omega|^2 = du^2 + dv^2$. The local indices, in this case, can be split as $\alpha = t, u, v$. From the metric Eq. (C1), one can easily read $\hat{\theta}^0 = v_F dt$, $\hat{\theta}^1 = \Lambda du$, and $\hat{\theta}^2 = \Lambda dv$, from where one can extract the components of the vielbeins e_μ^A . Now, from the Maurer-Cartan Eq. (1) and the torsionless condition, one can obtain $d\hat{\theta}^0 = 0$, and

$$d\hat{\theta}^1 + \frac{\Lambda_v}{\Lambda^2} \hat{\theta}^1 \wedge \hat{\theta}^2 = 0, \quad (\text{C2})$$

$$d\hat{\theta}^2 + \frac{\Lambda_u}{\Lambda^2} \hat{\theta}^2 \wedge \hat{\theta}^1 = 0. \quad (\text{C3})$$

Now, from Eq. (C2) one can deduce $\omega_0^1 = 0$ and $\omega_2^1 = \frac{\Lambda_v}{\Lambda^2} \hat{\theta}^1 + X \hat{\theta}^2$ for some local function X , whereas from Eq. (C3) one can deduce that $\omega_0^2 = 0$ and $\omega_1^2 = \frac{\Lambda_u}{\Lambda^2} \hat{\theta}^2 + \tilde{X} \hat{\theta}^1$. Now we use the metric condition $\omega^{AB} = -\omega^{BA}$; thus one can determine X and

\tilde{X} , turning that the only nonzero components of the connection one-form are

$$\omega^{12} = -\omega^{21} = \frac{\Lambda_v}{\Lambda^2} \hat{\theta}^1 - \frac{\Lambda_u}{\Lambda^2} \hat{\theta}^2. \quad (\text{C4})$$

These components expressed in local coordinates are given by $\omega_u^{12} = -\omega_u^{21} = \partial_v \log \Lambda(\omega)$ and $\omega_v^{12} = -\omega_v^{21} = -\partial_u \log \Lambda(\omega)$. Consequently, the spin connection Ω_α is given simply as $\Omega_t = 0$, $\Omega_u = \frac{i}{2} \partial_v \log \Lambda(\omega) \sigma_3$, and $\Omega_v = -\frac{i}{2} \partial_u \log \Lambda(\omega) \sigma_3$.

Now we use all this information to write an explicit expression for the Dirac equation in these space-times. Denoting the $2+1$ Dirac spinor by Ψ and making the transformation $\Psi = \Lambda^{-\frac{1}{2}} \Phi$, we can show that the Dirac equation is given by

$$i\hbar \partial_t \Phi = -i \frac{\hbar v_F}{\Lambda} (\sigma_1 \partial_u \Phi + \sigma_2 \partial_v \Phi). \quad (\text{C5})$$

In the simplest case, when $\Lambda = 1$, the above equations correspond to the Dirac equation in Minkowski's space-time. The Dirac equation in these coordinates u, v is particularly useful when the conformal factor Λ depends on one of the coordinates. Noticeably, Eq. (C5) is valid for any conformally flat space metric [22].

2. Natural coordinates for the catenoid

In this section, we write the Dirac equation in the most natural coordinates of the catenoid before considering the WE representation Eq. (3). Indeed, let us consider the parametrization of the catenoid obtained from the 2π -rotation of the catenary, that is,

$$\mathbf{X}(z, \varphi) = (R(z) \cos \varphi, -R(z) \sin \varphi, z), \quad (\text{C6})$$

where $\mathbf{R}(z) = R_0 \cosh(z/R_0)$, with R_0 the radius of the neck of the catenoid, where $z \in (-\infty, \infty)$, and $\varphi \in [0, 2\pi)$. The metric square line, in this case, is given by

$$ds^2 = R_0^2 \cosh^2 \left(\frac{z}{R_0} \right) \left(\frac{1}{R_0^2} dz^2 + d\varphi^2 \right). \quad (\text{C7})$$

Clearly, one can identify the coordinates $u \rightarrow \zeta = z/R_0$ and $v \rightarrow \varphi$, and the conformal factor $\Lambda(\omega) \rightarrow \lambda(\zeta) = R_0 \cosh(z/R_0)$. The expression Eq. (C5) is advantageous since the conformal factor depends on one of the coordinates. Further, it is convenient to define the following change of variables: $x = R_0 \sinh \zeta$, where $x \in (-\infty, \infty)$, thus it is not difficult to show that $\lambda^{-1}(\zeta)\partial_\zeta = \partial_x$. Indeed, the Dirac equation reduces to the equation found above Eq. (19), $i\hbar\partial_t\Phi = v_F\sigma_1\hat{p}_x\Phi + v_F\sigma_2V(x)\hat{\ell}_\varphi\Phi$, where $\hat{p}_x = -i\hbar\partial_x$ and $\hat{\ell}_\varphi = -i\hbar\partial_\varphi$ are linear and angular momentum operators, and the expected effective potential found above $V(x) = 1/\sqrt{x^2 + R_0^2}$. The connection between the natural coordinates and the polar coordinates can be accomplished by using the change of variable $r = e^\zeta$ and identified $\varphi \rightarrow \theta$.

APPENDIX D: EXPLICIT PARAMETRIZATIONS

In this section, we show explicit parametrizations for the catenoid, helicoid, B_1 -Bour, and the classical Enneper surfaces in polar coordinates (r, φ) , following Ref. [55]. For the catenoid

$$\mathbf{X}_c(r, \varphi) = \left(\frac{\alpha}{2} \left(\frac{1}{r} + r \right) \cos \varphi, \frac{\alpha}{2} \left(\frac{1}{r} + r \right) \sin \varphi, -\alpha \log r \right); \quad (D1)$$

for the helicoid

$$\mathbf{X}_h(r, \varphi) = \left(\frac{\beta}{2} \left(r - \frac{1}{r} \right) \sin \varphi, \frac{\beta}{2} \left(r - \frac{1}{r} \right) \cos \varphi; \beta \varphi \right), \quad (D2)$$

for the classical Enneper surface

$$\mathbf{X}_e(r, \varphi) = \left(r \cos \varphi - \frac{r^3}{3} \cos 3\varphi, -r \sin \varphi - \frac{r^3}{3} \sin 3\varphi, r^2 \cos 2\varphi \right), \quad (D3)$$

and for the B_1 -Bour surface

$$\mathbf{X}_b(r, \varphi) = \left(\log r - \frac{r^2}{2} \cos 2\varphi, -\varphi - \frac{r^2}{2} \sin 2\varphi, 2r \cos \varphi \right). \quad (D4)$$

Using these parametrizations, \mathbf{X}_c , \mathbf{X}_h , \mathbf{X}_b , and \mathbf{X}_e , we have drawn the surfaces inside Figs. 1, and 2, 4 with the help of MATHEMATICA.

-
- [1] K. S. Novoselov, D. Jiang, F. Schedin, T. J. Booth, V. V. Khotkevich, S. V. Morozov, and A. K. Geim, Two-dimensional atomic crystals, *Proc. Natl. Acad. Sci. USA* **102**, 10451 (2005).
- [2] B. Amorim, A. Cortijo, F. de Juan, A. Grushin, F. Guinea, A. Gutiérrez-Rubio, H. Ochoa, V. Parente, R. Roldán, P. San-Jose, J. Schiefele, M. Sturla, and M. Vozmediano, Novel effects of strains in graphene and other two dimensional materials, *Phys. Rep.* **617**, 1 (2016).
- [3] K. S. Novoselov, A. K. Geim, S. V. Morozov, D. Jiang, M. I. Katsnelson, I. V. Grigorieva, S. V. Dubonos, and A. A. Firsov, Two-dimensional gas of massless Dirac fermions in graphene, *Nature (London)* **438**, 197 (2005).
- [4] G. W. Semenoff, Condensed-matter simulation of a three-dimensional anomaly, *Phys. Rev. Lett.* **53**, 2449 (1984).
- [5] D. P. DiVincenzo and E. J. Mele, Self-consistent effective-mass theory for intralayer screening in graphite intercalation compounds, *Phys. Rev. B* **29**, 1685 (1984).
- [6] P. R. Wallace, The band theory of graphite, *Phys. Rev.* **71**, 622 (1947).
- [7] A. H. Castro Neto, F. Guinea, N. M. R. Peres, K. S. Novoselov, and A. K. Geim, The electronic properties of graphene, *Rev. Mod. Phys.* **81**, 109 (2009).
- [8] A. K. Geim and K. S. Novoselov, The rise of graphene, *Nat. Mater.* **6**, 183 (2007).
- [9] H. W. Kroto, J. R. Heath, S. C. O'Brien, R. F. Curl, and R. E. Smalley, c_{60} : Buckminsterfullerene, *Nature (London)* **318**, 162 (1985).
- [10] W. Krätschmer, L. D. Lamb, K. Fostiropoulos, and D. R. Huffman, Solid c_{60} : A new form of carbon, *Nature (London)* **347**, 354 (1990).
- [11] S. Iijima, Helical microtubules of graphitic carbon, *Nature (London)* **354**, 56 (1991).
- [12] H. Terrones and M. Terrones, Curved nanostructured materials, *New J. Phys.* **5**, 126 (2003).
- [13] P. Mélinon, Vitreous carbon, geometry and topology: A hollistic approach, *Nanomaterials* **11**, 1694 (2021).
- [14] H. Terrones and A. Mackay, The geometry of hypothetical curved graphite structures, *Carbon* **30**, 1251 (1992).
- [15] A. L. Mackay, H. Terrones, P. W. Fowler, H. W. Kroto, A. L. Mackay, G. Turner, and D. R. M. Walton, Hypothetical graphite structures with negative Gaussian curvature, *Philos. Trans. R. Soc. London, Ser. A* **343**, 113 (1993).
- [16] E. Braun, Y. Lee, S. M. Moosavi, S. Barthel, R. Mercado, I. A. Baburin, D. M. Proserpio, and B. Smit, Generating carbon schwarzites via zeolite-templating, *Proc. Natl. Acad. Sci. USA* **115**, E8116 (2018).
- [17] Y. Tanabe, Y. Ito, K. Sugawara, M. Koshino, S. Kimura, T. Naito, I. Johnson, T. Takahashi, and M. Chen, Dirac fermion kinetics in 3D curved graphene, *Adv. Mater.* **32**, 2005838 (2020).
- [18] M. Vozmediano, M. Katsnelson, and F. Guinea, Gauge fields in graphene, *Phys. Rep.* **496**, 109 (2010).
- [19] A. Iorio, Graphene: QFT in curved spacetimes close to experiments, *J. Phys.: Conf. Ser.* **442**, 012056 (2013).
- [20] A. Iorio, Graphene and black holes: Novel materials to reach the unreachable, *Frontiers Mater.* **1**, 1 (2015).
- [21] A. Iorio, Weyl-gauge symmetry of graphene, *Ann. Phys.* **326**, 1334 (2011).
- [22] M. Cvetič and G. W. Gibbons, Graphene and the Zermelo optical metric of the BTZ black hole, *Ann. Phys.* **327**, 2617 (2012).
- [23] A. Gallerati, Negative-curvature spacetime solutions for graphene, *J. Phys.: Condens. Matter* **33**, 135501 (2021).
- [24] A. Iorio and G. Lambiase, The Hawking-Unruh phenomenon on graphene, *Phys. Lett. B* **716**, 334 (2012).

- [25] A. Iorio and G. Lambiase, Quantum field theory in curved graphene spacetimes, Lobachevsky geometry, Weyl symmetry, Hawking effect, and all that, *Phys. Rev. D* **90**, 025006 (2014).
- [26] T. Morresi, D. Binosi, S. Simonucci, R. Piergallini, S. Roche, N. M. Pugno, and T. Simone, Exploring event horizons and hawking radiation through deformed graphene membranes, *2D Mater.* **7**, 041006 (2020).
- [27] B. S. Kandemir and d. Ertem, Quasinormal modes of BTZ black hole and hawking-like radiation in graphene, *Ann. Phys.* **529**, 1600330 (2017).
- [28] G. Volovik and M. Zubkov, Emergent Horava gravity in graphene, *Ann. Phys.* **340**, 352 (2014).
- [29] N. A. Shah, A. Contreras-Astorga, F. Fillion-Gourdeau, M. A. H. Ahsan, S. MacLean, and M. Faizal, Effects of discrete topology on quantum transport across a graphene $n-p-n$ junction: A quantum gravity analog, *Phys. Rev. B* **105**, L161401 (2022).
- [30] A. Iorio and P. Pais, Generalized uncertainty principle in graphene, *J. Phys.: Conf. Ser.* **1275**, 012061 (2019).
- [31] F. de Juan, A. Cortijo, and M. A. H. Vozmediano, Charge inhomogeneities due to smooth ripples in graphene sheets, *Phys. Rev. B* **76**, 165409 (2007).
- [32] A. Gallerati, Graphene, Dirac equation and analogue gravity, *Phys. Scr.* **97**, 064005 (2022).
- [33] A. J. Chaves, T. Frederico, O. Oliveira, W. de Paula, and M. C. Santos, Optical conductivity of curved graphene, *J. Phys.: Condens. Matter* **26**, 185301 (2014).
- [34] O. Oliveira, A. J. Chaves, W. de Paula, and T. Frederico, Signature of curved QFT effects on the optical properties of deformed graphene, *Europhys. Lett.* **117**, 27003 (2017).
- [35] D. V. Kolesnikov and V. A. Osipov, The continuum gauge field-theory model for low-energy electronic states of icosahedral fullerenes, *Eur. Phys. J. B* **49**, 465 (2006).
- [36] A. Cortijo and M. A. H. Vozmediano, Effects of topological defects and local curvature on the electronic properties of planar graphene, *Nucl. Phys. B* **763**, 293 (2007).
- [37] F. de Juan, M. Sturla, and M. A. Vozmediano, Space dependent Fermi velocity in strained graphene, *Phys. Rev. Lett.* **108**, 227205 (2012).
- [38] N. Levy, S. A. Burke, K. L. Meaker, M. Panlasigui, A. Zettl, F. Guinea, A. H. Castro Neto, and M. F. Crommie, Strain-induced pseudo-magnetic fields greater than 300 tesla in graphene nanobubbles, *Science* **329**, 544 (2010).
- [39] E. Arias, A. R. Hernández, and C. Lewenkopf, Gauge fields in graphene with nonuniform elastic deformations: A quantum field theory approach, *Phys. Rev. B* **92**, 245110 (2015).
- [40] P. Castro-Villarreal and R. Ruiz-Sánchez, Pseudomagnetic field in curved graphene, *Phys. Rev. B* **95**, 125432 (2017).
- [41] R. C. T. Da Costa, Quantum mechanics of a constrained particle, *Phys. Rev. A* **23**, 1982 (1981).
- [42] P. Schuster and R. Jaffe, Quantum mechanics on manifolds embedded in Euclidean space, *Ann. Phys.* **307**, 132 (2003).
- [43] G. Ferrari and G. Cuoghi, Schrödinger equation for a particle on a curved surface in an electric and magnetic field, *Phys. Rev. Lett.* **100**, 230403 (2008).
- [44] J. D. M. de Lima, E. Gomes, F. F. da Silva Filho, F. Moraes, and R. Teixeira, Geometric effects on the electronic structure of curved nanotubes and curved graphene: The case of the helix, catenary, helicoid, and catenoid, *Eur. Phys. J. Plus* **136**, 551 (2021).
- [45] V. Atanasov, R. Dandoloff, and A. Saxena, Geometry-induced charge separation on a helicoidal ribbon, *Phys. Rev. B* **79**, 033404 (2009).
- [46] Ö. Yeşiltaş, J. Furtado, and J. E. G. Silva, Dirac equation on a catenoid bridge: A supersymmetric approach, *Eur. Phys. J. Plus* **137**, 416 (2022).
- [47] L. N. Monteiro, C. A. S. Almeida, and J. E. G. Silva, Dirac fermions on wires confined to the graphene Möbius strip, *Phys. Rev. B* **108**, 115436 (2023).
- [48] R. Dandoloff, A. Saxena, and B. Jensen, Geometry-induced potential on a two-dimensional section of a wormhole: Catenoid, *Phys. Rev. A* **81**, 014102 (2010).
- [49] R. Dandoloff and T. Truong, Quantum hall-like effect on strips due to geometry, *Phys. Lett. A* **325**, 233 (2004).
- [50] M. S. Morris and K. S. Thorne, Wormholes in spacetime and their use for interstellar travel: A tool for teaching general relativity, *Am. J. Phys.* **56**, 395 (1988).
- [51] J. Silva, J. Furtado, T. Santiago, A. C. Ramos, and D. da Costa, Electronic properties of bilayer graphene catenoid bridge, *Phys. Lett. A* **384**, 126458 (2020).
- [52] B. S. DeWitt, Quantum field theory in curved spacetime, *Phys. Rep.* **19**, 295 (1975).
- [53] V. Atanasov and A. Saxena, Helicoidal graphene nanoribbons: Chiraltronics, *Phys. Rev. B* **92**, 035440 (2015).
- [54] P. Castro-Villarreal and J. Guven, Inverted catenoid as a fluid membrane with two points pulled together, *Phys. Rev. E* **76**, 011922 (2007).
- [55] J. K. Whittemore, Minimal surfaces applicable to surfaces of revolution, *Ann. Math.* **19**, 1 (1917).
- [56] U. Dierkes, S. Hildebrandt, and F. Sauvigny, *Minimal Surfaces* (Springer, Berlin-Heidelberg, 2010), pp. 53–90.
- [57] L. E. Parker and D. J. Toms, *Quantum Field Theory in Curved Spacetime: Quantized Fields and Gravity* (Cambridge University Press, New York, 2009).
- [58] M. Nakahara, *Geometry, Topology and Physics*, Graduate Student Series in Physics (Taylor and Francis, New York, 2003).
- [59] S.-S. Chern, An elementary proof of the existence of isothermal parameters on a surface, *Proc. Am. Math. Soc.* **6**, 771 (1955).
- [60] R. Osserman, Global properties of classical minimal surfaces, *Duke Math. J.* **32**, 565 (1965).
- [61] It is noteworthy to mention that usually the down valley sector, Ψ_{\downarrow} , is coupled with Dirac matrices transposed; however, one always can perform a global pseudospin SU(2) transformation on this sector such that one can use the same matrices as the up valley sector.
- [62] J. González, F. Guinea, and M. Vozmediano, The electronic spectrum of fullerenes from the Dirac equation, *Nucl. Phys. B* **406**, 771 (1993).
- [63] J. Gonzalez and J. Herrero, Graphene wormholes: A condensed matter illustration of dirac fermions in curved space, *Nucl. Phys. B* **825**, 426 (2010).
- [64] P. E. Lammert and V. H. Crespi, Graphene cones: Classification by fictitious flux and electronic properties, *Phys. Rev. B* **69**, 035406 (2004).
- [65] A similar procedure can be done in the Cartesian coordinates (see Appendix C).

- [66] B. A. Lippmann and J. Schwinger, Variational principles for scattering processes. I, *Phys. Rev.* **79**, 469 (1950).
- [67] J. J. Sakurai, *Modern Quantum Mechanics (Revised Edition)*, 1st ed. (Addison-Wesley, New York, 1994).
- [68] I. S. Gradshteyn and I. M. Ryzhik, *Table of Integrals, Series, and Products*, 7th ed., translated from Russian, edited and with a preface by A. Jeffrey and D. Zwillinger (Elsevier/Academic Press, Amsterdam, 2007), pp. xlviii+1171.
- [69] A. S. de Castro, $n+1$ dimensional Dirac equation and the Klein paradox, *Am. J. Phys.* **69**, 1111 (2001).
- [70] J. Fonseca, W. Moura-Melo, and A. Pereira, Scattering of charge carriers in graphene induced by topological defects, *Phys. Lett. A* **374**, 4359 (2010).
- [71] P. M. Morse and H. Feshbach, *Methods of Theoretical Physics Part I and II* (McGraw Hill Book Company, Inc., New York, 1953).